JOURNAL OF MATERIALS SCIENCE 27 (1992) 5994–6016

Second phase volume fraction and rubber particle size determinations in rubber-toughened polymers: a simple stereological approach and its application to the case of high impact polystyrene

C. MAESTRINI, M. MERLOTTI, M. VIGHI, E. MALAGUTI
Enichem Polimeri, Mantova Research Centre, Via Giuseppe Taliercio 14, 46100 Mantova, Italy

The determination of the volume fraction ϕ and of the particle size distribution $F(R)$ of the rubbery phase is necessary in many rubber-toughened polymers. High impact polystyrene is a good model system in which such a determination has to be performed *a posteriori*. The more commonly used procedures, i.e. phase-separation methods, analysis of micrographs and indirect mechanical measurements, all present drawbacks and difficulties. A simple stereological method, in which some of these difficulties are avoided, is proposed for the determination of ϕ and of some features of $F(R)$ from the analysis of micrographs. The validity of the method is tested by means of a wide numerical simulation. The proposed method, together with a standard phase-separation procedure and with indirect, mechanical measurements, is tested experimentally on two series of high impact polystyrene and the collected data are compared and discussed. The results of this investigation suggest that approximate views relating elastic properties of rubber-toughened materials only to the rubber particle volume fraction, however this parameter has been measured, not considering the size, the morphology and/or the structure of the rubber particles, are possibly questionable.

1. Introduction

Many two-phase materials are composed of a matrix in which a population of well dispersed, approximately spherical particles is embedded; focusing on plastics, one can find a very large number of polymeric materials of this kind. It is well known that a successful strategy to improve the toughness of a brittle polymer involves the addition to it of many small rubber particles [1]: this is the case, for example, for high impact polystyrene (HIPS), consisting of a matrix of polystyrene (PS) and of polybutadiene rubber particles, with diameters ranging from about 0.1 μm up to several μm.

When a stable, preformed second phase is used, the determination of the size distribution of the particles is relatively easy to attain and the assessment of the dispersed phase volume fraction in the final product is just a matter of knowing the mixture proportions. However, in other cases, the second phase is produced during the polymerization of the matrix, as for HIPS, or formed during the final manufacturing steps, as, for instance, in the case of the polymeric blends obtained by melt mixing. So the analysis of the second phase content, ϕ, and/or of the particle size distribution function, $F(R)$ (intended to be the frequency density distribution of the particle radius normalized over the whole positive range) can be performed only *a posteriori*, i.e. on the final two-phase material.

Henceforth attention will be concentrated particularly on HIPS, which is a good, simple model for a two-phase system that needs an *a posteriori* determination of the second phase features; this does not mean, however, that the conclusions presented in this work can only apply to HIPS. In HIPS the rubbery phase formation ordinarily takes place during the process of bulk-polymerization and follows the stage of phase inversion [1, 2]. Because of this manufacturing procedure, the second phase particles in the final product are generally composed of polybutadiene (PB), styrene–butadiene graft and/or block copolymer and by polystyrenic sub-inclusions: their size and number depend on several process parameters [1, 2].

The characteristics of the rubbery second phase in HIPS influence the elastic modulus, the stress at the yielding point and the fracture toughness [3, 4]. Thus, the dimensions of the composite particles play a very important role in the global mechanical performance: if the particles are too small, with diameter of about 0.1–0.2 μm or less, they appear to be ineffective as toughening agents [1, 4–6], but they may contribute again to the toughening mechanism if a very small

0022-2461

number of big particles is also present [7–9]. So, an optimum particle size and distribution has to be sought. From this, it plainly follows that a useful understanding and control of the HIPS mechanical behaviour cannot avoid the characterization of its dispersed phase. More generally, the mechanical performance of all rubber-toughened polymeric systems depends in a decisive way on their inner morphology; there is a great need, then, to find precise experimental tools to determine ϕ and $F(R)$.

In this paper we briefly review and analyse the HIPS second phase characterization procedures proposed and used in the past, showing how some factors have always been neglected. Then, we present a method, based on simple stereological principles, allowing reliable results to be obtained quickly from the image analysis of the material micrographs. (Stereology refers to the class of mathematical methods for reconstructing the parameters defining a material structure in space from measured values obtained on a section of the structure.) A computer simulation and a wide experimental application of the method are also presented and discussed.

2. Second phase characterization methods for HIPS

Two different approaches are mainly reported in the literature, concerning the characterization of the second phase in HIPS and in other similar rubber-toughened systems. The first consists in the material separation, normally achieved by the selective solution of the PS matrix, and then in the characterization of the separated, insoluble phase, usually called *gel*. The second one is based, in contrast, on the characterization of the bulk material and normally uses the methods of image analysis applied to optical microscopy (OM) or to electron microscopy micrographs.

2.1. Phase separation methods

A method typically used to determine the HIPS second phase volume fraction is the Ruffing gel test [10]. In this procedure the material is dissolved in toluene and the rubbery phase is isolated by centrifugation. The toluene is then removed from the isolated, wet gel by heating under negative pressure. The ratio between the dry rubbery phase and the weight of the original sample is assumed to be the second phase weight fraction from which the second phase volume fraction is easily computed, taking the densities into account.

The procedure introduced by Cigna [3] is, in principle, the same. A sample of HIPS is dissolved in a mixture of 57% toluene and 43% methyl ethyl ketone (MEK). After centrifugation at 6000 r.p.m. the insoluble part is separated as a swollen gel and needs to be washed, at least twice, with fresh solvent. The gel is then coagulated in methanol and dried overnight in an oven at 40 °C. Again the ratio between the weight of the dried gel and that of the original sample is considered to be the second phase weight fraction.

Separation methods involving the extraction of the rubber particles from the matrix are widely used also in the determination of the particle size distribution. A dry gel, produced by a method similar to those described above, can easily be observed with an optical microscope or a scanning electron microscope (SEM) and histograms reproducing the detected frequency versus the observed radius or diameter of the particles are obtainable from the micrographs [8]. Measurements are also possible directly on the solution in which the gel particles are suspended: this is the case, for example, in the low angle light scattering [11] and in the Coulter Counter experiments [12–14], which allow an estimation of the particle size distribution.

All these procedures have some problems. The first is that of solvent choice: a procedure like, for example, the one proposed in Ref. 3 gives somewhat different values of gel weight for different solvents [15]. A possible cause lies in the fact that the PS sub-inclusions could be extracted from the particles in different proportions by different solvents. However, all the authors that used the selective solvent method implicitly assumed that no extraction of the sub-inclusions had taken place. Another problem arises from the centrifugation. As Hall [16] demonstrated, the amount of rubber particles centrifuged depends on the rubbery phase cross-linking and on the rubber particle size: small particles are more difficult to centrifuge and the centrifugation efficiency increases as the rubbery phase cross-linking increases.

These two difficulties, together with the fact that the particles could be partially swollen also after drying, affect the precision of the measurements of the volume fraction and of the particle size distribution as well. Similarly, the particle size distribution measurements made in solution take account of particles swollen by the solvent in which they are suspended and then a correction factor has to be applied, or the suspension has to be modified, replacing the solvent with a non-swelling liquid.

Even if the indicated obstacles can be partially overcome, the phase-separation methods still have a major, unavoidable drawback: the division of the material into its constitutive phases necessarily involves severe physico-chemical manipulations, which could change its morphological characteristics. The features of the separated gel could be extremely different from those of the second phase in the bulk, and, to be sure of the data accuracy, a cross-check is definitely needed.

Finally, a more subtle issue can be addressed: presumably in HIPS a non-negligible amount of PS-PB graft and/or block copolymer lies on the interface between matrix and particles and it cannot be dissolved by the PS-selective solvents, giving its contribution to the gel and to the particle size distribution measurements. However, it is questionable whether from a mechanical point of view, the interfacial PS branches or blocks should be computed in the rubbery phase. The graft and/or block copolymer is responsible for the adhesion between matrix and particles and, therefore, it is reasonable to assume that the particle size cannot be completely independent of the quantity of this interfacial material. Thus one can expect, as a very first approximation, that small particles could be associated with high interfacial tension and, consequently, with a considerable relative amount of interfacial matter. So, the fact that the PS part of the interfacial copolymer is computed in the gel could cause difficulties when trying to correlate the phase-separated volume fraction data with the mechanical properties, particularly when dealing with samples containing small particles. In the Experimental section of this work this point will be discussed further, adding to the above qualitative considerations some experimental evidence.

2.2. Microscopy characterization methods

The characterization of the second phase of the bulk materials requires the observation of the features of the two phases when they are tangled together in the solid state. This is usually by means of microscopy methods. Only techniques connected with OM and with transmission electron microscopy (TEM) will be discussed here, leaving some short considerations about SEM analysis and measurements to the next section.

The first necessity for a microscopic survey is that of cutting from the sample a slice suitable for the observation, i.e. transparent or partially transparent to the light or to the electron beam. For HIPS, the maximum thickness that one can utilize in OM is about 5–7 μm, while in TEM at 100 kV a sample 1 μm thick is already extremely dark. On the other hand, using sophisticated techniques of ultramicrotomy or of cryo-ultramicrotomy, the thinnest feasible HIPS slices are of about 0.07 μm. So, it is clear that the thickness of the sample, which could span two magnitude orders, is not an insignificant variable and cannot be neglected, particularly when quantitative measurements are claimed to be made.

Next, it is important that the second phase could be distinguished from the matrix. This is achieved by the use of the phase contrast technique in OM and by several staining procedures in TEM, all derived from the original one developed by Kato using osmium tetroxide (OsO_4) [17].

In phase contrast illumination, invisible retardation of phase due to slight variations in refractive index is converted to visible changes in light intensity, resulting in increased image contrast. The phase contrast is best for specimens with only very slight differences in the refractive indices. But, for PS and PB at room temperature, the refractive indices n_D are 1.60 and 1.52, respectively and thus their difference is quite large. This, together with the poor achievable magnification, makes the identification of the phase boundaries in HIPS not really easy by OM.

The staining techniques are based on the fact that the staining agent chemically reacts with a portion of the sample. This results not only in the addition of the heavy atom to the rubber phase, which provides contrast for TEM, but also in the cross-linking of the rubber, which makes it rigid enough to allow room temperature microtomy and increases the stability of the sample in the electron beam. The Kato staining technique is widely applied, giving rise to very good images; however, caution must be used, owing to the extreme toxicity of OsO_4. It has to be noted, finally, that the staining agent can swell the particles, changing somewhat their dimensions [18].

Following one of the described procedures, appropriate micrographs of the material can be taken, with the limit for the OM that the maximum achievable magnification, requiring oil-immersed objective lenses, is about 2500 × . The micrographs, which are two-dimensional projections of the spatial two-phase arrangement present in the considered slices, show, as a rule, a bunch of approximately circular (sometimes overlapped) section which represent the rubber particles (see, for example, the TEM micrographs of HIPS in the Experimental section of this paper (Figs 10–12)). To reconstruct the second phase features, i.e. ϕ and $F(R)$, from such micrographs is a matter of image analysis and of properly taking into account the stereology of the process that gave rise to the microscopic observation.

A basic rule of stereology is the Delesse–Rosiwal principle for areal and linear analysis. According to this principle, the volume fraction of a second phase randomly embedded in a structure is equal, under some, very broad, conditions, to its areal or linear fraction obtained on an ideal section, i.e. on a section with zero thickness [19]. This principle has been sometimes applied to the micrographs for the determination of ϕ, not taking into account, however, the fact that the pictures always concern sections with a finite thickness t. We will show in the next section that the error involved in doing so is the greater the lower the ratio between the average particle size and t and that it becomes particularly critical when thick slices and/or small particles are under investigation.

Bucknall and co-workers [20] considered the problem of the thickness of the slice, using the following formula, proposed by Underwood [21]:

$$\phi = \frac{4R}{4R + 3t}\phi_{\text{app}} \tag{1}$$

where ϕ is the second phase volume fraction in the bulk, ϕ_{app} the apparent volume fraction in the considered section, t the section thickness and R the particle radius. Bucknall, in reality, did not propose exactly Equation 1; he replaced parameter R with $\bar{R}$, defining it as the mean particle radius. In that form the equation is not strictly true. It must be said, in fact, that Equation 1 applies only to the case of a monomodal distribution of particles randomly arranged in space, i.e. to the case in which the material contains particles having all the same radius equal to R (in this paper the term "monomodal" will always have this precise meaning). If the particle size distribution is not monomodal, Equation 1 slightly changes its form, as will be seen in the next section. However, there is a more important ambiguity in this work; it is not clear how Equation 1 could be applied, as claimed, without trying to reconstruct the bulk particle size distribution from the two-dimensional distribution and without estimating the key parameter R.

Concerning the determination of $F(R)$, it is clear that the problem of the reconstruction of the bulk particle size distribution from their two-dimensional section radius or diameter distribution must be recognized. The problem can be analytically solved considering a distribution of spheres. Goldsmith [22] generalized a method developed by Wicksell [23, 24], considering an infinite section having thickness t. He derived a Volterra integral equation of the second kind for the relationship between the distribution of section radius, $f(r)$ (intended to be the frequency density distribution of the particle section radius normalized over the whole positive range, in analogy with $F(R)$), and the distribution of the spheres, $F(R)$

$$f(r) = \frac{t}{(t + 2\bar{R})} F(r) + \frac{2r}{(t + 2\bar{R})} \int_{r}^{R_{\max}} \frac{F(R)\,dR}{\sqrt{R^2 - r^2}} \tag{2}$$

where $R_{\max}$ is the largest sphere radius and $\bar{R}$ is the mean radius*. As in the more general case of all the integral equations, the handling of Equation 2 is not an easy matter. Experimentally one can arrive at merely a quite precise estimation of t and discretized approximation of $f(r)$, generally in the form of a histogram. Also bypassing the mathematical problems of existence and uniqueness of the solution function $F(R)$, this allows only the numerical solutions of Equation 2, i.e. following the method proposed by Goldsmith himself, to write and solve an elaborate system in order to reconstruct an histogram for $F(R)$.

As far as we know, no effort has been made by polymer scientists to apply Equation 2 to the determination of $F(R)$. Only Bucknall [20] mentioned a simplified version of the equation (with $t = 0$), but did not attempt to solve it. The usual approach, adopted by almost all the authors, consists, in fact, in extracting only qualitative information concerning $F(R)$ from the histograms of $f(r)$, obtained by the micrographs.

2.3. Other characterization methods

Other methods, which cannot be classified exactly as phase separation or microscopy and image analysis, have been used in the determination of the second phase characteristics of HIPS.

Some authors utilized SEM on microtomed or fractured surfaces [25], sometimes using etching to enhance the surface topography. Because the etching process generally involves a selective dissolution of the sample constituents or chemical reactions whose rates are different in the two phases, it faces, in principle, the same drawbacks that affect the phase separation methods. Moreover, the SEM images have to be processed, from a stereological point of view, as the TEM images, with the simplification that the slice thickness can be considered, to a sufficient approximation, zero. Nevertheless, as far as we know, no incontestable analysis of SEM data has been, up to now, presented in the literature.

Another possibility is, for example, that of determining the second phase volume fraction from the features of the peaks in the loss factor versus temperature curves [26, 27]. However, it has been shown that ideas with regard to the rubber peak size as relating to the rubber concentration or to the second phase volume content are complicated by additional considerations about the composition, morphology and methods of preparation of the materials [28].

Cigna [3] and later Bucknall *et al.* [20, 29, 30] noted that the elastic modulus of HIPS depends on the total second phase volume fraction, including also the polystyrenic rigid sub-inclusions. More theoretical studies substantially confirmed this view, demonstrating that the difference in the mechanical elastic behaviour between a system composed of entirely soft particles and another one, containing rigid particles only surrounded by a soft shell, is negligible [31, 32]. The elastic modulus, then, could be an appropriate measure of the rubbery phase volume fraction, but there is no clear evidence that this could be true for all particle structures and morphologies. It is also clear that such a determination needs a calibration curve and therefore cannot be considered as an absolute, independent method.

3. Mathematical model

3.1. Description

As indicated in the previous section, the solution of the Volterra Equation 2 requires complex mathematical tools which are often over-sized for the purpose and the accuracy of the measurements involved in the rubber-toughened polymers characterization. However, one definitely needs to have information concerning $F(R)$ and a quite precise estimation of ϕ. In this section, then, a simple mathematical model is presented, based on very intuitive stereological assumptions, which allows information to be obtained about $F(R)$ and ϕ without requiring intricate computational procedures.

In this section an ideal two-phase material composed of a matrix and a population of spheres randomly arranged in space but distributed according to $F(R)$ in size will always be considered and the existence of a microscopic procedure is assumed which enables micrographs to be obtained from variably thick, but large enough sections where the phase boundaries could be exactly recognizable. A micrograph is intended to be, from a mathematical point of view, simply the two-dimensional projection of the considered section (see Fig. 1).

The radius of the ith particle is represented as R_i and its apparent radius in the projection as r_i. It is obvious that, when the whole particle or at least its equatorial region is contained in the section, one has $r_i = R_i$; on the other hand, when the particle is cut by

---

* It must be stressed that the particles are assumed to be arranged in size according to $F(R)$, but randomly arranged in space. This means that their centres do not lie in any particular lattice layout. In fact, if one imagines particles distributed, for example, in a perfect cubic lattice it is possible to have planes in which no particle sections are visible (interplanar surfaces), violating both Equations 1 and 2.

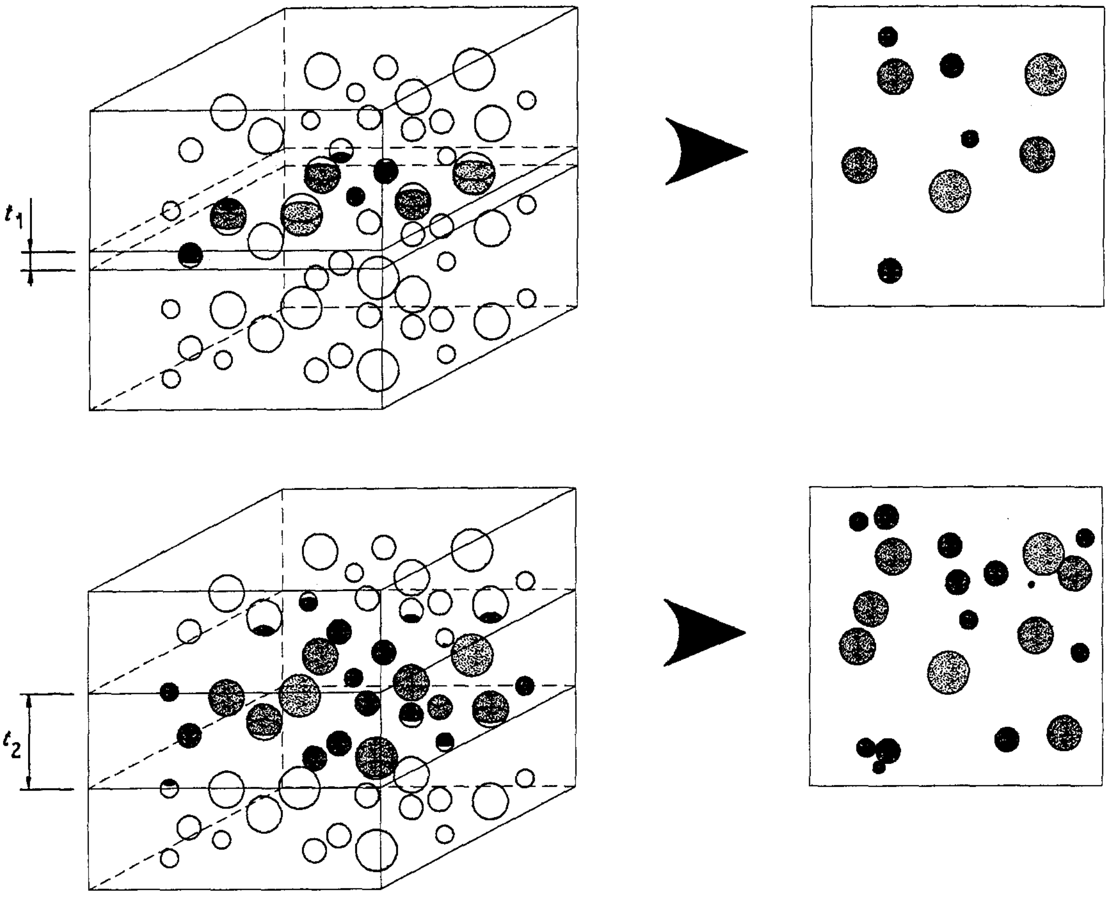

Figure 1 A cube of an ideal material containing an embedded population of spherical particles is sketched. (a) The cube is cut with a section having thickness t_1 and the arrow shows the corresponding view in which the particle sections are visible. (b) The same cube is cut with a thicker section with thickness t_2 and the corresponding view contains a larger number of visible particle sections.

the section excluding its equatorial region, $r_i < R_i$ holds. Thus, the thinner the considered section, the greater the difference between the particle size distribution in the bulk and in the micrographs.

On the other hand, it is easy to recognize that increasing the section thickness from zero to infinity, the apparent volume fraction of the second phase, i.e. the areal volume fraction, will increase correspondingly from the bulk volume fraction value (Delesse–Rosiwal principle) to 1 (Fig. 1).

To take into account quantitatively the described qualitative effects, a few definitions that will be useful in the following have here to be introduced. Consider a large enough volume region containing M particles and assume that the number of particles could be representative of the total distribution. Let the ath (a is a positive integer) moment of the radius distribution $F(R)$ about zero be called $\langle R^a \rangle$, defined as

$$\langle R^a \rangle = \frac{\sum_{i=1}^{M} R_i^a}{M} \tag{3}$$

By analogy the bth (b is a positive integer) moment of the section radius distribution $f(r)$ about zero, is the value $\langle r^b \rangle$ provided by

$$\langle r^b \rangle = \frac{\sum_{j=1}^{N} r_j^b}{N} \tag{4}$$

where r_j represents the apparent radius of the jth particle contained in a given section and N is considered to be sufficiently large that the number of the observed particles could be representative of the distribution $f(r)$ in an infinite section. Clearly the first moment of a distribution represents the number average value of the distribution or, in other words, the mean value.

For simplicity, let us start from the case in which all the particles have the same radius R and the considered section has zero thickness, i.e. it is a mathematical surface. It is evident that, for all a positive integers, the following relationship holds

$$\langle R^a \rangle = R^a \tag{5}$$

The surface will intersect N particles, each of them will present a circular section whose radius r_j will range from 0 to R, depending on the distance between the particle centre and the surface itself. The section radius distribution moments $\langle r^b \rangle$ must now be calculated. To do that it is helpful to recognize that the sections on the surface are exactly distributed as the sections cut by planes on a single particle (see Fig. 2)*. If we imagine, at this point, a single sphere cut by N parallel planes equally spaced by ε, i.e.

$$N\varepsilon = 2R \tag{6}$$

the problem becomes that of the computation of the

---

* We do not demonstrate this equivalence, which has to be accepted as intuitively evident. Indirect confirmations of the rightness of the approach will be given in the following.

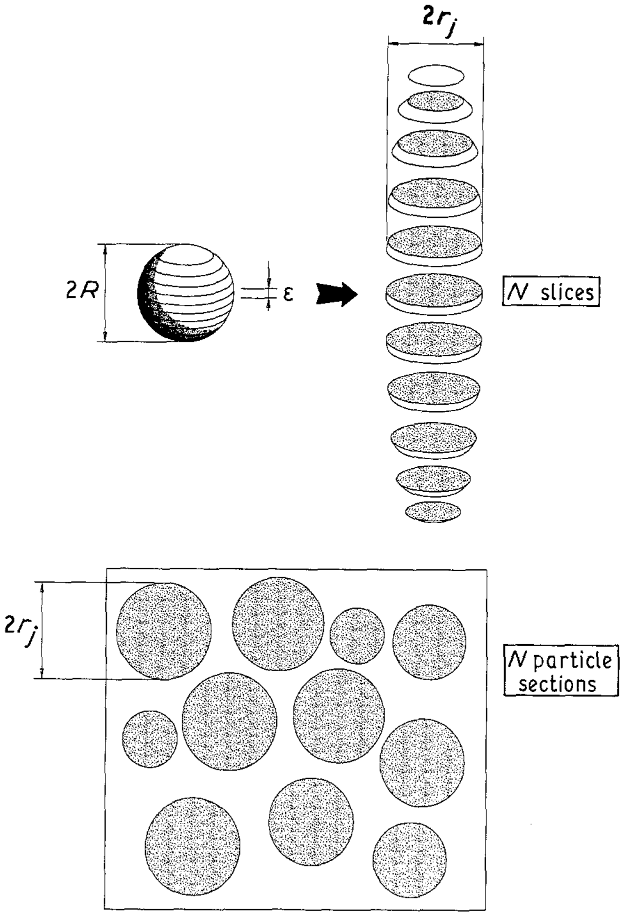

Figure 2 The particle sections on a surface are distributed as the sections cut by planes on a single particle (monomodal distribution).

section radius distribution moments cut by these planes (the moments are defined exactly as in Equation 4, with self-evident adjustments in the meaning of the symbols).

Referring to Fig. 2, two equations, concerning a (vertical) surface, A, and the volume, V, of the considered particle, can be written

$$A = \pi R^2 \sim \sum_{j=1}^{N} 2\varepsilon r_j = 2N\varepsilon\left(\frac{\sum_{j=1}^{N} r_j}{N}\right) = 2N\varepsilon\langle r^1\rangle \qquad (7)$$

$$V = \frac{4\pi R^3}{3} \sim \sum_{j=1}^{N} \varepsilon(\pi r_j^2) = N\varepsilon\pi\left(\frac{\sum_{j=1}^{N} r_j^2}{N}\right) = N\varepsilon\pi\langle r^2\rangle \qquad (8)$$

Taking Equation 6 into account, it is easy to recognize that Equations 7 and 8 become, respectively

$$\langle r^1\rangle \sim \frac{\pi R}{4} \qquad (9)$$

$$\langle r^2\rangle \sim \frac{2R^2}{3} \qquad (10)$$

Clearly, Equations 9 and 10 are exact equations when the double limit $N \to \infty$ and $\varepsilon \to 0$ is executed.

From the last two relationships one can easily conclude that the mean radius in the section is lower than the radius of the particles in the bulk; this is due to the process of cutting, which introduces into the projection particle sections having radii lower than R. Moreover, in the examined case, the Delesse–Rosiwal principle states that the apparent areal volume fraction coincides with the three-dimensional volume fraction.

Now the more complex case must be considered in which the section radius distribution moments have to be computed on micrographs relative to specimens having finite thickness t, supposing again a monomodal distribution of particles. Once more, the situation can be assumed equivalent to the computation of the maximum section radius distribution moments cut on a single particle, instead of by a single surface, by two planes at a distance t one from the other.

To make it clearer, let us imagine the particle in space and choose a direction, so that it could be possible to indicate the regions above and below the sphere. Let P_t and P_b be the top and bottom planes considered, having a vertical coordinate difference t, and imagine that the two planes, initially placed above the sphere, come down. They will start to intersect the particle when P_b will reach the upper pole of the sphere. The maximum sections between the two planes, which are those of interest for the computation, will be detached by P_b up to moment in which it will go beyond the particle equator. The equator, then, will stay between P_t and P_b and the radius R will be computed as the maximum section radius until P_t will surpass it too. Eventually, the sections cut by P_t will be the maximum sections.

It is quite easy to recognize now that the sections contained in a large micrograph with thickness t are exactly distributed as the sections cut by planes on a single, composite figure formed by an upper and a lower half-sphere, with radius R, and by a central cylinder with the same radius R and height equal to t.

Imagine this figure again cut by N parallel planes equally spaced with a distance ε:

$$N\varepsilon = 2R + t \qquad (11)$$

The problem, as before, becomes that of the computation of the section radius distribution moments cut by these planes. Two equations, concerning the area of a (vertical) surface, A, and the volume, V, of the composite figure, in analogy with Equations 7 and 8, can be written

$$A = \pi R^2 + 2tR \sim \sum_{j=1}^{N} 2\varepsilon r_j = 2N\varepsilon\left(\frac{\sum_{j=1}^{N} r_j}{N}\right) = 2N\varepsilon\langle r^1\rangle \qquad (12)$$

$$V = \frac{4\pi R^3}{3} + \pi t R^2 \sim \sum_{j=1}^{N} \varepsilon(\pi r_j^2) = N\varepsilon\pi\left(\frac{\sum_{j=1}^{N} r_j^2}{N}\right) = N\varepsilon\pi\langle r^2\rangle \qquad (13)$$

Taking into account Equation 11, Equations 12 and

13 become, respectively

$$\langle r^1 \rangle \sim \frac{\pi R^2 + 2tR}{4R + 2t} \qquad (14)$$

$$\langle r^2 \rangle \sim \frac{4R^3 + 3tR^2}{6R + 3t} \qquad (15)$$

The double limit $N \to \infty$ and $\varepsilon \to 0$ makes Equations 14 and 15 exact equations, as above. It is also easily recognizable that Equations 14 and 15 are reduced to Equations 9 and 10 when t is zero.

For the computation of the apparent areal volume fraction, ϕ_{app}, a cube of material with volume L^3 must be considered. Supposing that the cube contains M particles, the bulk second phase volume fraction, ϕ, will be estimated as

$$\phi = \frac{4\pi M R^3}{3L^3} \qquad (16)$$

It is possible, then, to introduce the number of particles per unit volume, M_{v}, given by

$$M_{\mathrm{v}} = \frac{M}{L^3} \qquad (17)$$

Let us consider a section with thickness t and parallel to one side of the cube. This section will intersect the particles with centre included in the section itself or not further than R from one of the section surfaces. In order correctly to take into account all the particles intersected by this section, it must be assumed that the section has an effective volume, V_{e}, given by

$$V_{\mathrm{e}} = L^2(2R + t) \qquad (18)$$

The number of particles, N, included in V_{e} will simply be

$$N \sim M_{\mathrm{v}} V_{\mathrm{e}} = \frac{M(2R + t)}{L} \qquad (19)$$

Because of the mathematical treatment developed above, the particles included in V_{e} can be assumed to all have the same maximum areal section equal to $\pi\langle r^2 \rangle$. So, the total surface covered by the areal section of the particles, S, will be

$$S \sim \pi N \langle r^2 \rangle \qquad (20)$$

At this point ϕ_{app} can be easily computed as

$$\phi_{\mathrm{app}} = S L^{-2} \qquad (21)$$

and then, using Equations 15, 16 and 20

$$\phi_{\mathrm{app}} \sim \frac{4R + 3t}{4R}\phi \qquad (22)$$

which is equivalent to Equation 1, considering the limit $L \to \infty$.

The above approach can be generalized for any particle size distribution $F(R)$ (the outlines of this generalization are sketched in Appendix 1 of this paper) and Equations 14, 15 and 22 assume the more general form

$$\langle r^1 \rangle = \frac{\pi\langle R^2 \rangle + 2t\langle R^1 \rangle}{4\langle R^1 \rangle + 2t} \qquad (23)$$

$$\langle r^2 \rangle = \frac{4\langle R^3 \rangle + 3t\langle R^2 \rangle}{6\langle R^1 \rangle + 3t} \qquad (24)$$

$$\phi_{\mathrm{app}} = \frac{4\langle R^3 \rangle + 3t\langle R^2 \rangle}{4\langle R^3 \rangle}\phi \qquad (25)$$

with the implicit assumption that the previously mentioned limits should all be considered.

3.2. Geometrical meaning of Equations 23, 24 and 25

It is necessary to know how the features of the particle distribution in the bulk $F(R)$ and the thickness t of the considered slice affect the distribution $f(r)$ in the section. First, it is convenient to introduce some parameters that have a clear geometrical significance and that are easily related to the above defined moments. One can check that $\langle R^1 \rangle$, $\langle R^2 \rangle$ and $\langle R^3 \rangle$ can be rewritten as

$$\langle R^1 \rangle = \bar{R} \qquad (26)$$

$$\langle R^2 \rangle = \bar{R}^2(1 + \beta^2) \qquad (27)$$

$$\langle R^3 \rangle = \bar{R}^3(1 + 3\beta^2 + \gamma\beta^3) \qquad (28)$$

where $\bar{R}$ and the two coefficients, independent of the units in which $F(R)$ is measured, β and γ, defined as

$$\bar{R} = \langle R^1 \rangle \qquad (29)$$

$$\beta^2 = \frac{\sum_{i=1}^{M} (R_i - \langle R^1 \rangle)^2}{\langle R^1 \rangle^2} = \frac{\sigma^2}{\langle R^1 \rangle^2} \qquad (30)$$

$$\gamma = \frac{\sum_{i=1}^{M} (R_i - \langle R^1 \rangle)^3}{\beta^3\langle R^1 \rangle^3} \qquad (31)$$

have an exact geometrical meaning: $\bar{R}$ is the mean radius, β, simply related to the standard deviation σ, is a measure of the dispersion of the considered distribution (the larger β, the broader the distribution) and, finally, γ is an estimation of the skewness of the distribution (if γ assumes positive values, it indicates an excess of large positive deviations from the mean value, if γ is zero the distribution is symmetrical around the mean value and if γ is negative there is an excess of large negative deviations). It is important to remark at this point that the two parameters β and γ cannot vary arbitrarily; in fact, large values of β coupled to large negative values of γ imply, from a mathematical point of view, that $F(R)$ assumes non-zero, positive values also when R is negative, which is, of course, without any physical and geometrical sense. So, one has always to deal with low values of β and γ. Reasonable distributions are particularly characterized by β below 1 and by γ not greater than a few units in absolute value. Of course, $\langle r^1 \rangle$ and $\langle r^2 \rangle$ can also be interpreted by analogy as the mean radius and as a measure of the relative broadness of the apparent distribution.

Equations 23, 24 and 25 can then be edited in the following form

$$\rho_1 = \frac{\langle r^1 \rangle}{\bar{R}} = \frac{\pi(1 + \beta^2)\tau + 2}{4\tau + 2} \qquad (32)$$

$$\rho_2 = \frac{\langle r^2 \rangle}{\bar{R}^2} = \frac{4(1 + 3\beta^2 + \gamma\beta^3)\tau + 3(1 + \beta^2)}{6\tau + 3} \tag{33}$$

$$\frac{\phi_{\text{app}}}{\phi} = 1 + \frac{3(1 + \beta^2)}{4(1 + 3\beta^2 + \gamma\beta^3)\tau} \tag{34}$$

where the parameter τ, defined as:

$$\tau = \frac{\bar{R}}{t} \tag{35}$$

is a measure of the relative thinness of the considered specimen (the higher the value of τ, the thinner the section with respect to the included particles). The content of Equations 32, 33 and 34 can be directly clarified using some graphs.

Fig. 3 shows a three-dimensional plot of ρ_1 versus τ and β. The parameter ρ_1 is the mean radius of the distribution $f(r)$ with respect to the mean radius of the bulk distribution $F(R)$. Then, if it assumes values inferior to 1, it means that particle sections with apparent radius lower than $\bar{R}$ are preponderant in the apparent distribution $f(r)$. From Fig. 3 it is easy to conclude that, for small values of τ, the apparent mean radius $\langle r^1 \rangle$ tends to be the same as $\bar{R}$, independently of β, i.e. independently of the dispersion of $F(R)$. This is quite clearly understandable if one realizes that low values of τ imply that very thick sections, which can contain a large number of non-cut particles, are under observation. In this case, in fact, the apparent radius must coincide with the real one.

Increasing τ the ratio ρ_1 changes, with different slopes corresponding to different β. Notably, this change is strong particularly in the range of τ which is of experimental interest for the characterization of HIPS and of several other two-phase polymeric materials; assuming a section thickness of 0.2–0.3 μm, which is a reasonable value for a TEM specimen, the largest variation of ρ_1 will take place corresponding to a range of particles having mean radius between 2 μm and 0.05 μm, which is the very range in which the rubber particles present in many rubber-toughened materials are contained. It is important to remark also that the dependence of ρ_1 on β indicates that the broader the distribution in the bulk, the larger the apparent mean radius in the section results, giving rise to the noteworthy fact that very large distributions have a larger mean apparent radius in thin slices than in thick ones. Finally, it has to be added that the skewness of the bulk distribution $F(R)$ does not influence the mean radius in the section.

Fig. 4 is a three-dimensional plot of ρ_2 versus τ and β, keeping γ constant and equal to zero, i.e. considering only symmetric distributions. The parameter ρ_2 can be considered as an evaluation of the relative dispersion of the distribution $f(r)$, so the fact that it increases with increasing β for all values of τ is understandable making the reasonable assumption that broad distributions in the bulk will give rise to broad distributions in the sections. It is noticeable also that the dependence of the broadness of $f(r)$ on β is higher for large values of τ, i.e. when thin slices are under consideration. In thin slices, in fact, the original dispersion β has to be added to the one resulting from the cutting. Again, the region of τ of experimental interest is the one in which the bigger variations in the parameter ρ_2 take place.

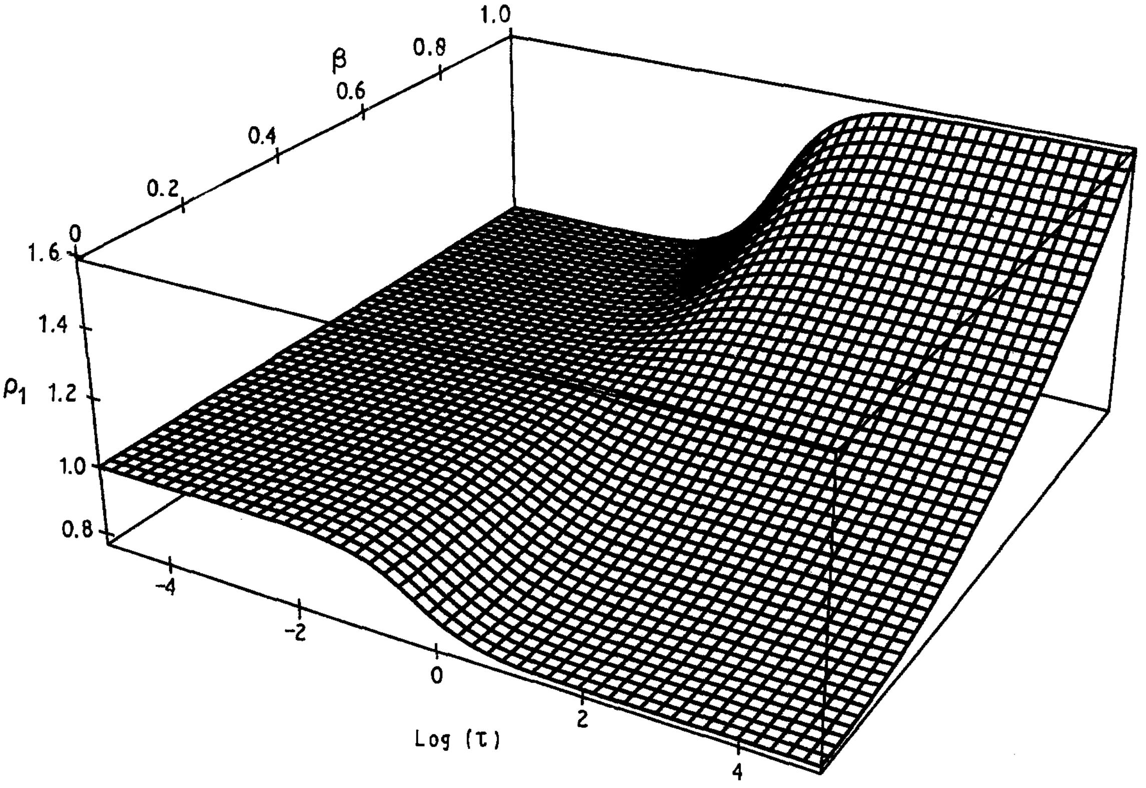

Figure 3 Three-dimensional plot of ρ_1 versus $\log\tau$ and β.

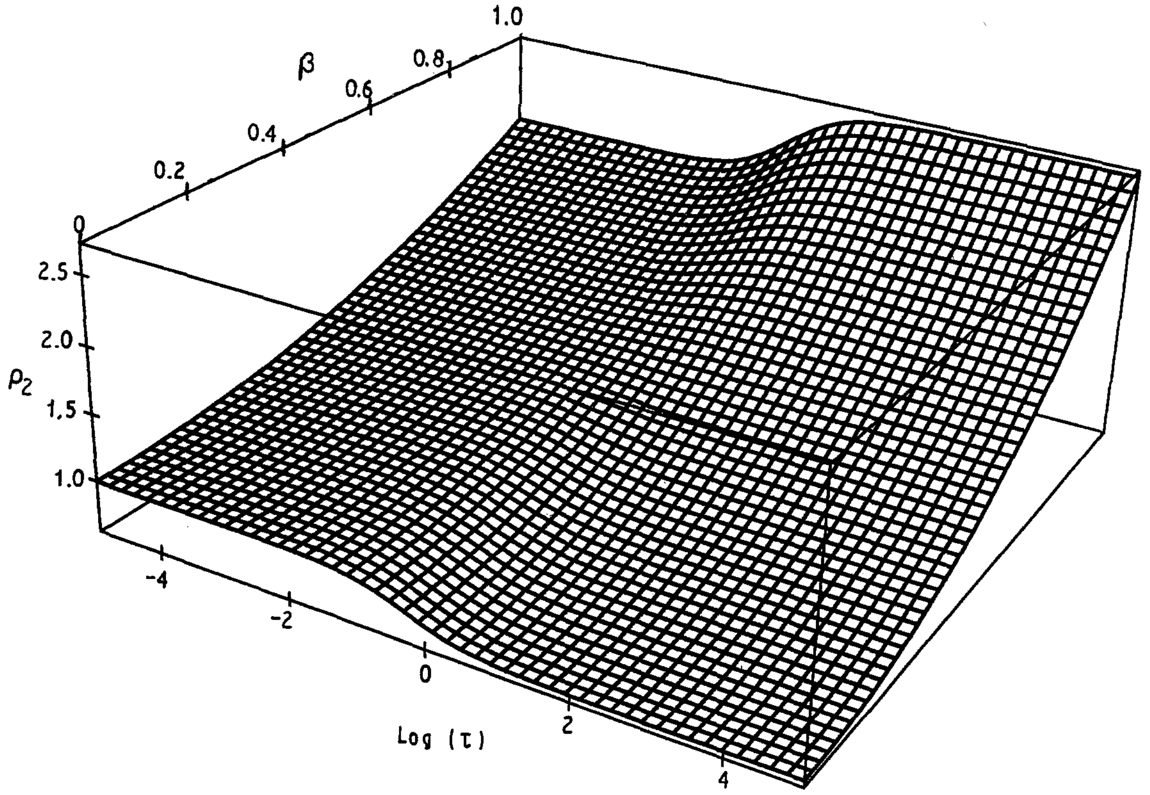

Figure 4 Three-dimensional plot of ρ_2 versus $\log\tau$ and β, keeping $\gamma = 0$.

Fig. 5 is a three-dimensional plot of ρ_2 versus τ and γ in which, this time, β has been kept constant and positive. When thick slices, containing several non-cut particles, are observed the broadness of $f(r)$ should depend only on the broadness β of the bulk distribution and should not be affected by the skewness of $F(R)$. In fact the value of ρ_2 does not depend on γ for very low values of τ. On the other hand, when τ is larger, we observe that distributions that are negatively skewed in the bulk appear less dispersed than the symmetrical or the positively skewed ones. This is a good demonstration of the fact that the process of cutting influences in a complex way the resulting distribution.

Eventually, we come to discuss how ϕ_{app}/ϕ changes with varying τ. Fig. 6 shows the three-dimensional plot of ϕ_{app}/ϕ versus τ and β, keeping γ constant and equal to zero i.e. considering only symmetric distributions. For high τ the ratio ϕ_{app}/ϕ does not depend on β and tends to 1, according to the previously mentioned Delesse–Rosiwal principle.

On the other hand, when τ tends to zero the parameter ϕ_{app}/ϕ tends to infinity: this means that ϕ_{app} could have values larger than 1, which is without any geometrical significance. This is because it was not taken into consideration that, in a thick slice, many particle sections can overlap (the problem of the possible overlapping of the particle projections in the section is discussed in its quantitative terms in Appendix 2).

Anyway, from the observation of Fig. 7, one can conclude that the broadness of a generic, symmetric distribution does not affect significantly the parameter ϕ_{app}/ϕ and that the considerable slope variation in ϕ_{app}/ϕ takes place only for low values of τ.

The situation partially changes when one comes to consider skewed distributions. In Fig. 7ϕ_{app}/ϕ is plotted versus τ and γ, keeping β constant and positive. Again, no dependence on γ can be observed when τ is high, always according to the Delesse–Rosiwal principle; however, for low values of τ, the skewness slightly affects the slope of the curves: increasing γ the value of ϕ_{app} tends to decrease with respect to ϕ and this effect takes place in the range of practical interest.

3.3. Application of Equations 23, 24 and 25

From a given, sufficiently large micrograph coming from a sample with known thickness t, it is possible to compute $\langle r^b \rangle$, with b a positive integer, and ϕ_{app}. So Equations 23, 24 and 25 have four unknowns, i.e. $\langle R^1 \rangle$, $\langle R^2 \rangle$, $\langle R^3 \rangle$ and ϕ. To reduce the system to linearity and for more simplicity, one can recognize that, if $\langle R^1 \rangle$, $\langle R^2 \rangle$ and $\langle R^3 \rangle$ are known, ϕ is easily computable from Equation 25. The problem can then be limited to consider only Equations 23 and 24, which are linear in the unknowns $\langle R^1 \rangle$, $\langle R^2 \rangle$ and $\langle R^3 \rangle$. Even so, we have at this point a linear system of only two equations and three unknowns, which is in general not solvable.

In Appendix 1 the generic equation giving the expression for $\langle r^k \rangle$, with $k > 2$, is derived. However, adding further equations for the higher moments of $f(r)$ does not help in the solution of the linear system. In fact, the generic $\langle r^k \rangle$ is given as a function $\langle R^1 \rangle$, $\langle R^k \rangle$ and $\langle R^{k+1} \rangle$, then the number of the unknowns is always higher than that of the equations. This impasse can be avoided if it is assumed that the particle distribution function $F(R)$ has specific, known

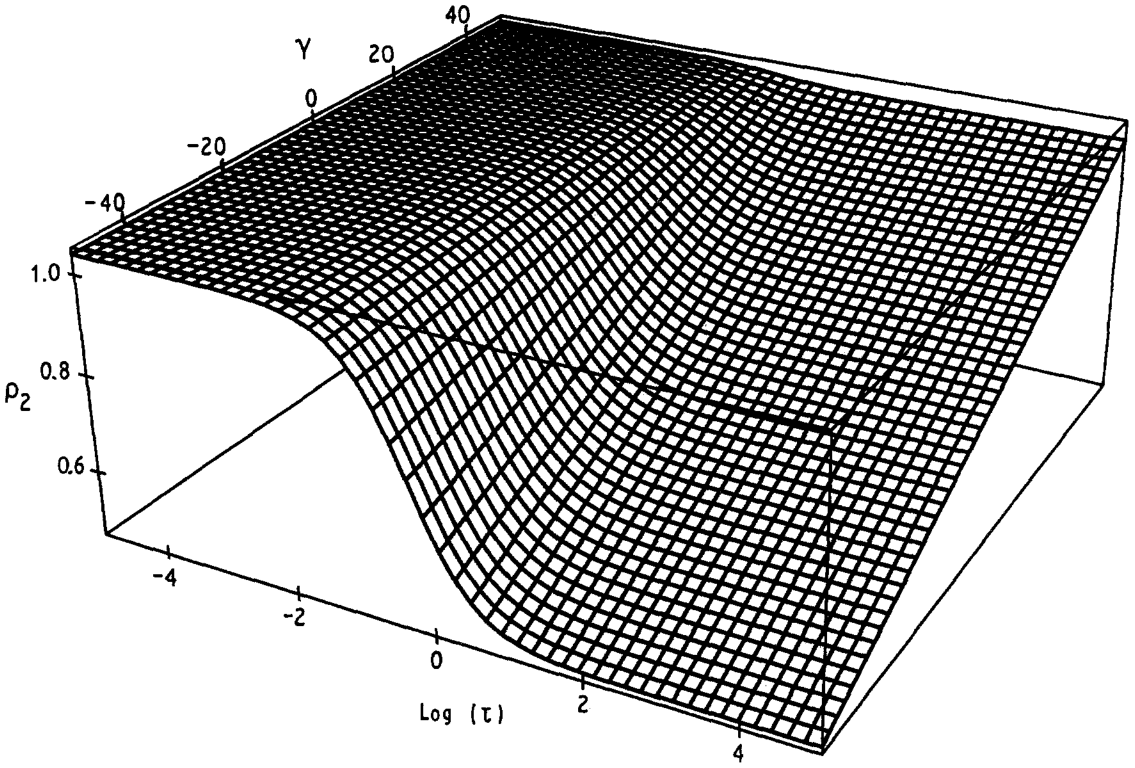

Figure 5 Three-dimensional plot of ρ_2 versus log(τ) and γ, keeping $\beta = 0.2$.

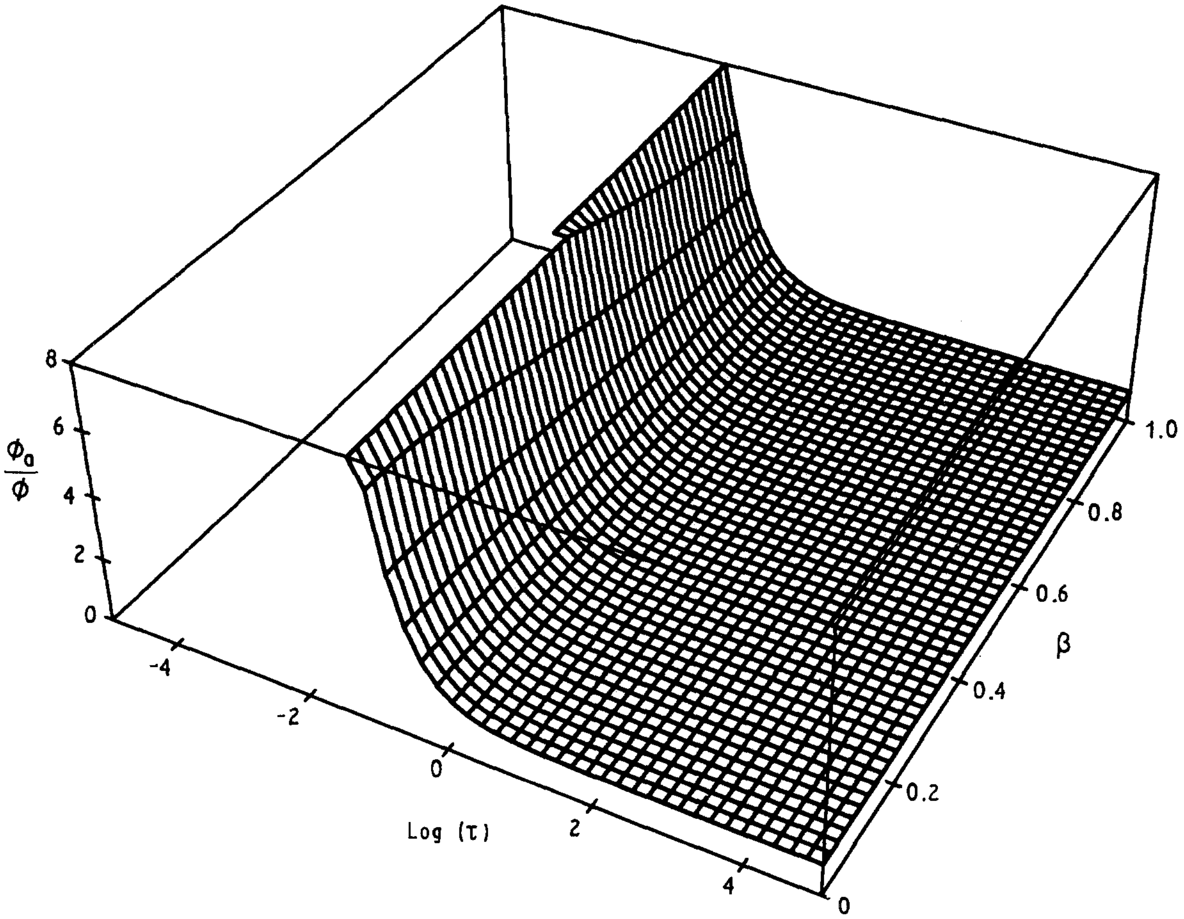

Figure 6 Three-dimensional plot of ϕ_{app}/ϕ versus τ and β, keeping $\gamma = 0$. For low values of τ, ϕ_{app}/ϕ tends to increase beyond the limits of the box in which the plot is contained and then no surface is plotted in that region.

features, for example that it is monomodal or log-normal, as some distributions in rubber-toughened polymers are supposed to be: in this case to Equations 23 and 24 a generic relationship can be added of the form $g(\langle R^1\rangle, \langle R^2\rangle, \langle R^3\rangle) = 0$, making the system at least numerically computable.

Nevertheless, there is a simpler possibility, which avoids non-experimental assumptions and makes it

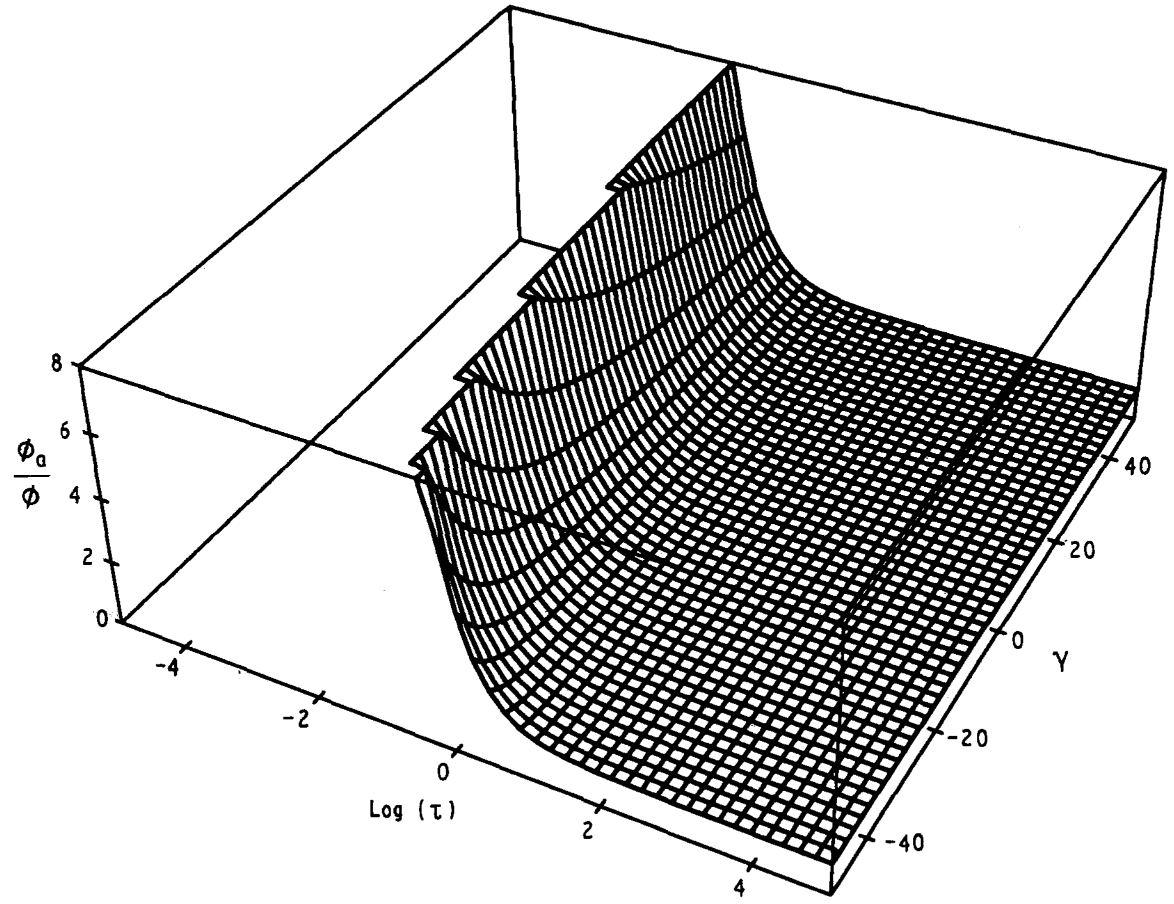

Figure 7 Three-dimensional plot of ϕ_{app}/ϕ versus τ and γ, keeping $\beta = 0.275$. For low values of τ, ϕ_{app}/ϕ tends to increase beyond the limits of the box in which the plot is contained and then no surface is plotted in that region.

possible to deal only with linear, easily solvable systems. If, in fact, several measurements of the parameters are made on pictures from samples having different thickness t_i, the number of equations increases: namely if, from the same material, n different cuts have been done, a system of $2n$ equations with three unknowns can be written from Equations 23 and 24

$$t_1\colon\ a_{1,1}\langle R^1\rangle + a_{1,2}\langle R^2\rangle + a_{1,3}\langle R^3\rangle = b_1 \quad (36)$$

$$a_{2,1}\langle R^1\rangle + a_{2,2}\langle R^2\rangle + a_{2,3}\langle R^3\rangle = b_2 \quad (37)$$

$$t_2\colon\ a_{3,1}\langle R^1\rangle + a_{3,2}\langle R^2\rangle + a_{3,3}\langle R^3\rangle = b_3 \quad (38)$$

$$a_{4,1}\langle R^1\rangle + a_{4,2}\langle R^2\rangle + a_{4,3}\langle R^3\rangle = b_4 \quad (39)$$

$$t_n\colon\ a_{2n-1,1}\langle R^1\rangle + a_{2n-1,2}\langle R^2\rangle + a_{2n-1,3}\langle R^3\rangle = b_{2n-1} \quad (40)$$

$$a_{2n,1}\langle R^1\rangle + a_{2n,2}\langle R^2\rangle + a_{2n,3}\langle R^3\rangle = b_{2n} \quad (41)$$

where the coefficients $a_{i,j}$ and b_i are easily computable when n different thicknesses t_i are considered.

When $n > 1$ the system is clearly overdetermined: there are more equations than unknowns. To state the situation in a matricial form we have:

$$A\langle \mathbf{R}\rangle = b \quad (42)$$

where A and b have the obvious meaning of the system coefficient matrix and column vector and $\langle \mathbf{R}\rangle$ is the column vector

$$\langle \mathbf{R}\rangle = \begin{pmatrix} \langle R^1\rangle \\ \langle R^2\rangle \\ \langle R^3\rangle \end{pmatrix} \quad (43)$$

Saying that the system is overdetermined is equal to stating that the matrix A has more lines than columns. Strictly speaking, then, Equation 42 will not have solutions, unless some lines in A are linearly dependent, and such a system is called *non-consistent*. However, overdetermined systems are often encountered during experimental work and several procedures exist that give useful results. All the methods deal with the so called rest vector, s, defined as

$$s = A\langle \mathbf{R}\rangle - b \quad (44)$$

Because, in general, it is impossible to make s equal to zero, one can attempt to choose $\langle \mathbf{R}\rangle$ in order to make s minimum in some way.

The easiest procedure (the one that will be followed in the Experimental section) is the least squares method, which consists in finding $\langle \mathbf{R}\rangle$ that makes minimum the quantity $s^T \cdot s$, where s^T is the line vector transposed from s and the multiplication dot is intended for the standard matricial multiplication. It is simple to demonstrate that this is equivalent to solving the system

$$(a_1, a_1)\langle R^1\rangle + (a_1, a_2)\langle R^2\rangle + (a_1, a_3)\langle R^3\rangle = (a_1, b) \quad (45)$$

$$(a_2, a_1)\langle R^1 \rangle + (a_2, a_2)\langle R^2 \rangle + (a_2, a_3)\langle R^3 \rangle = (a_2, b) \quad (46)$$

$$(a_3, a_1)\langle R^1 \rangle + (a_3, a_2)\langle R^2 \rangle + (a_3, a_3)\langle R^3 \rangle = (a_3, b) \quad (47)$$

where (a_i, a_j), defined as

$$(a_i, a_j) = a_{1,i}a_{1,j} + a_{2,i}a_{2,j} + \ldots + a_{2n,i}a_{2n,j} \quad (48)$$

is clearly the scalar product between the two column vectors a_i and a_j.

We mention here another widely used method: the Çebyshev or *min–max* method, into the details of which we need not go. It is sufficient to remember that this method consists of choosing $\langle \mathbf{R} \rangle$ in order that the maximum component of the rest vector s should be minimum. The system is then transformed in a series of linear disequations that can be treated using the routines of linear programming such as, for example, the *simplex* algorithm. It could be, finally, useful to remember that the *min–max* method is more appropriate than the least squares one when there are one or a few components of the rest vector that tend to be markedly larger than the others or when further conditions have to be associated with the system.

4. Numerical simulation

Because some of the assumptions made in the previous section have only an intuitive foundation, it is important to check the validity of the formulae thus derived using an independent method before applying them to practical cases. The process of cutting and that of image production can be easily simulated using a computer program, so we developed one in FORTRAN, the general outlines of which are sketched in this section. The program can be divided in two main parts: the first concerning the input procedure and the routine for the particle arrangement and the second strictly limited to the elaboration.

4.1. Input

The program consists in constructing the Cartesian simulation of a cube of material containing several particles and then in splitting one or more sections of defined thickness on which the requested computations are made. The algorithm that we used then requires, as input parameters,

- the volume fraction ϕ of the second phase,
- the approximate number M of particles to be considered in our simulated cube of material,
- information about the particle size distribution $F(R)$.

We considered only monomodal, pseudo-random, normal and log-normal distributions but, as will be clear in the following, the algorithm can easily be adapted for all the distributions that have a $F(R)$ which can be expressed in analytical form.

4.1.1. Monomodal distribution

This is the simplest case: the radius R is the only parameter to be introduced. The program, then, will consider M particles all having the same radius R.

4.1.2. Pseudo-random distribution

In this case the radius of the particles is assumed to be distributed randomly from a minimum value $R_{\min}$ and a maximum value $R_{\max}$. The program uses, for each of the M particles to be introduced, a generator of pseudo-random numbers calibrated between $R_{\min}$ and $R_{\max}$ in order to assess the radius.

4.1.3. Normal distribution

The expression of $F(R)$ for a normal distribution is

$$F(R) = \frac{1}{\sqrt{2\pi}\sigma} \exp\left(-\frac{(R - \bar{R})^2}{2\sigma^2} \right) \quad (49)$$

where $\bar{R}$ is the mean radius and σ the standard deviation. It is important to observe that the normal distribution, being symmetrical around the mean value, always has positive values of F corresponding to negative values of R, which does not have geometrical meaning in our specific case. Let us, then, consider the distribution only in a positive interval given in standard deviation units as $[\bar{R} - N_\sigma\sigma, \bar{R} + N_\sigma\sigma]$ with $(\bar{R} - N_\sigma\sigma) > 0$. If we divide this interval into N_{cl} sub-intervals each of length equal to ΔR and centre coordinate R_i, the normalization property of $F(R)$ implies that

$$\sum_{i=1}^{N_{\text{cl}}} F(R_i)\Delta R \sim 1 \quad (50)$$

when the distribution does not possess considerable queues for large values of $(R - \bar{R})^2$ and when N_{cl} tends to infinity. The value ΔR can be easily termed as

$$\Delta R = \frac{2N_\sigma\sigma}{N_{\text{cl}}} \quad (51)$$

then Equation 50 becomes

$$\sum_{i=1}^{N_{\text{cl}}} F(R_i)\frac{2N_\sigma\sigma}{N_{\text{cl}}} \sim 1 \quad (52)$$

We said that the purpose of the program is to introduce in the considered cube of material M particles, whose radii should be distributed according to $F(R)$. If we consider the same N_{cl} radius intervals mentioned above, the number n_i of particles having radius R_i inside the ith interval has to satisfy the condition

$$\sum_{i=1}^{N_{\text{cl}}} n_i \sim M \quad (53)$$

At this point it is easy to recognize, from the previous equations, that the number of particles to be introduced in the class having mean radius R_i is

$$n_i \sim \frac{2MN_\sigma\sigma}{N_{\text{cl}}} F(R_i) \quad (54)$$

The program then requires as input parameters:

- The mean radius of the normal distribution $\bar{R}$,
- the standard deviation of the normal distribution σ,
- the amplitude of the interval in which the distribution is considered (in standard deviation units) $2N_\sigma$,
- the number of classes in which the considered interval is divided N_{cl},

and, for each radius R_i defined as:

$$R_i = \bar{R} - N_\sigma\sigma + \frac{2iN_\sigma\sigma}{N_{cl}} \tag{55}$$

it introduces a number of particles corresponding to that given in Equation 54. Of course this discretized distribution in size will better mimic the continuous normal distribution as the ratio $(2MN_\sigma\sigma)/N_{cl}$ increases.

4.1.4. *Log-normal distribution*

The so-called log-normal distribution is a distribution normal when the x-axis is plotted on a logarithmic scale. The expression for $F(R)$ in this case is the following

$$F(R) = \frac{1}{\sqrt{2\pi}\sigma_L R}\exp\left\{\frac{-(lnR - \bar{R}_L)^2}{2\sigma_L^2}\right\} \tag{56}$$

where $\bar{R}_L$ and σ_L are parameters characterizing the mean value and the standard deviation of the distribution in logarithmic scale. It is easy to calculate that the mean value $\bar{R}$ and the standard deviation σ are instead given by

$$\bar{R} = \exp\left(\bar{R}_L + \frac{\sigma_L^2}{2}\right) \tag{57}$$

$$\sigma = (\exp(2\bar{R}_L + \sigma_L^2)(\exp(\sigma_L^2) - 1))^{1/2} \tag{58}$$

Therefore an approach similar to that developed for the normal distribution, using $\bar{R}$ and σ, can be adapted when a given log-normal distribution has to be discretized.

4.2. Particle arrangement

The program now possesses M particles for which it has memorized the radius R_i distributed according to the selected distribution $F(R)$. The distribution moments can then be easily computed according to the formulae given in the previous section and the particles have to be arranged in space.

The program chose to dispose the particles inside a cube having Cartesian coordinates $0 \leq x_i \leq L$ ($i = 1, 2, 3$). The cube edge is computed as

$$L = \left(\frac{4\pi\langle R^3\rangle M}{3\phi}\right)^{1/3} \tag{59}$$

consistently with all the input data. Then, using a pseudo-random number generator calibrated between 0 and L, the centre coordinates $(x_1(i), x_2(i), x_3(i))$ of each ith particle are generated, taking into account that all the particles must be contained in the considered cube:

$$(j = 1, 2, 3), \forall i = 1, 2, 3, \ldots M \quad (x_j(i) - R_i) \geq 0 \tag{60}$$

$$(j = 1, 2, 3), \forall i = 1, 2, 3, \ldots M \quad (x_j(i) - R_i) \leq L \tag{61}$$

and that the particles cannot overlap

$\forall i, \forall j = 1, 2, 3, \ldots M$

$$\sqrt{\sum_{k=1}^{3}(x_k(i) - x_k(j))^2} \leq R_i + R_j \tag{62}$$

The easiest way, from the programming point of view, to get the three above conditions satisfied is to iterate the use of the random number generator each time that the centre coordinates produced do not meet the requirements. Of course, when a large number of particles is considered and/or when we are trying to simulate a material having a considerable value of second phase volume fraction, this method becomes dramatically time-consuming because it has to find free spaces inside the particle arrangement only by random guessing. In these cases some simple strategies can be developed, like, for example, introducing bigger particles first.

4.3. Elaboration

The elaboration part of the program is dedicated to the simulation of the cutting and image analysis processes. For simplicity we choose to have the slices cut along planes parallel to the first two axes. Always using the pseudo-random number generator the mean third coordinate h of the slice is introduced with the restriction that the whole thick slice should be contained in the cube, i.e.

$$h - \frac{t}{2} \geq 0 \tag{63}$$

$$h + \frac{t}{2} \leq L \tag{64}$$

The computation of the section moments $\langle r^b\rangle$ (b is a positive integer) and of the apparent volume fraction ϕ_{app} follows simply by determining which particles are completely or partially included in the section.

From a mathematical point of view the generic jth particle for which the two conditions

$$x_3(j) - R_j < h + \frac{t}{2} \tag{65}$$

$$x_3(j) + R_j > h - \frac{t}{2} \tag{66}$$

are satisfied gives its contribution both to the section moments and to the apparent volume fraction. Of course, if in the cube we have M particles, the particles satisfying Equations 65 and 66 will be N with $N \leq M$. From now then we will consider only these N.

When the jth particle has its equatorial region contained in the section, i.e. when

$$x_3(j) \geq h - \frac{t}{2} \tag{67}$$

$$x_3(j) \leq h + \frac{t}{2} \tag{68}$$

are satisfied, it is easy to conclude that

$$r_j = R_j \tag{69}$$

On the other hand, the section will cut the particle off from its equatorial region: in this case the following expression gives the value of the apparent radius

$$r_j^2 = \max\left\{\left[R_j^2 - \left(x_3(j) - h + \frac{t}{2}\right)^2\right] \times \left[R_j^2 - \left(x_3(j) - h - \frac{t}{2}\right)^2\right]\right\} \tag{70}$$

So the moments and the apparent volume fraction can be computed as

$$\langle r^b \rangle = \frac{\sum_{j=1}^{N} r_j^b}{N} \tag{71}$$

$$\phi_{\text{app}} = \frac{\pi \sum_{j=1}^{N} r_j^2}{L^2} \tag{72}$$

If the precision in the computation has to be increased one can choose to examine more than one section.

The values obtained from Equations 71 and 72 do not have any relationship with Equations 23, 24 and 25, so the simulation can be considered a test for their validity.

Many simulations have been performed; they involved all the four different particle size distributions described, with different combinations of parameters so that variably large and skewed distributions have been tested (always more than 2000 particles in the section have been considered) and consistently an excellent agreement has been found between the theoretical values estimated by Equations 23, 24 and 25 and those computed using Equations 71 and 72. Figs 8 and 9 show the accord between the data from the simulations and the theoretical relationships in the simple case of monomodal distributions.

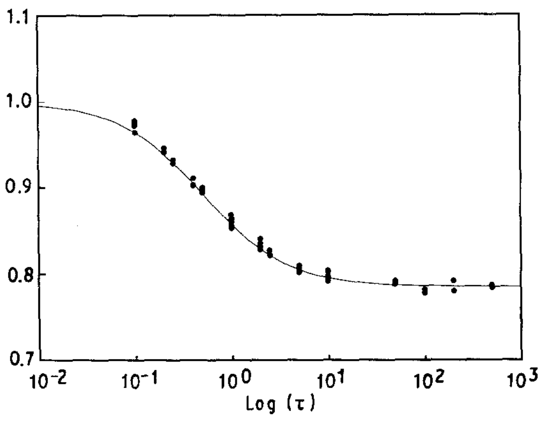

Figure 8 Plot of ρ_1 versus $\log\tau$. The solid line represents the theoretical relationship from Equation 32 and the symbols are data from the numerical simulation. The simulation concerned only monomodal distributions.

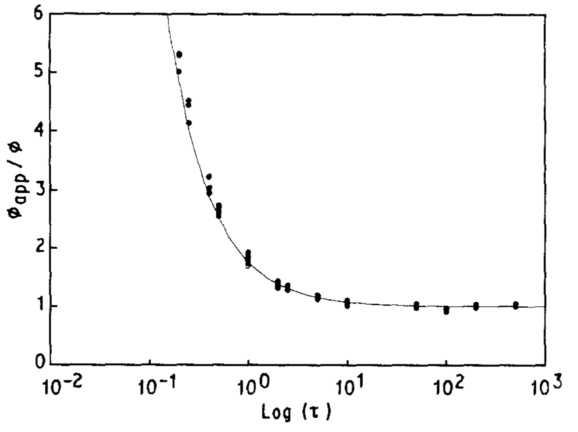

Figure 9 Plot of ϕ_{app}/ϕ versus $\log\tau$. The solid line represents the theoretical relationship from Equation 34 and the solid circles are data from the numerical simulation. The simulation concerned only monomodal distributions.

5. Experimental procedure

The main conclusion drawn in the previous sections was that the thickness of the observed slices becomes a very important parameter in image analysis, especially when the ratio between the mean particle radius and the thickness itself varies from about 0.1 to 10, which is the range of practical interest for many rubber-toughened materials observed by TEM.

An impressive confirmation of the great influence that the thickness of the samples has on the final features of micrographs is given in Figs 10 and 11. The two pictures come from the same material (the characteristics of which will be described in the following), cut in slices having different thicknesses, lower and higher, respectively. For instance, it is immediately seen that the apparent volume fraction is extremely different in the two pictures. So far, there is a real, practical need to take into account the factors analysed in the previous sections.

In this section an experimental work will be described on two series of different HIPS: attention will be concentrated on the second phase volume fraction measurement, using for its determination different and independent methods, the first of which is the one based on the approach of image analysis previously developed.

5.1. Materials

Two different HIPS were studied, indicated in the following simply as HIPS1 and HIPS2, containing particles having very different size and structure. In HIPS1 (see Fig. 12) the particles are relatively big, with the so-called "salami" structure, while the particles in HIPS2 (see Figs 10 and 11) are smaller, exhibiting the more simple "core–shell" structure.

The different dimensions and structure of the particles in the two materials are obtained during the polymerization process; it is important to remark that a very critical role is played by the amount and nature of the matter at the interface between bulk PS and particles, which, of course, will be in some ways different in the two materials. From the HIPS1 and HIPS2

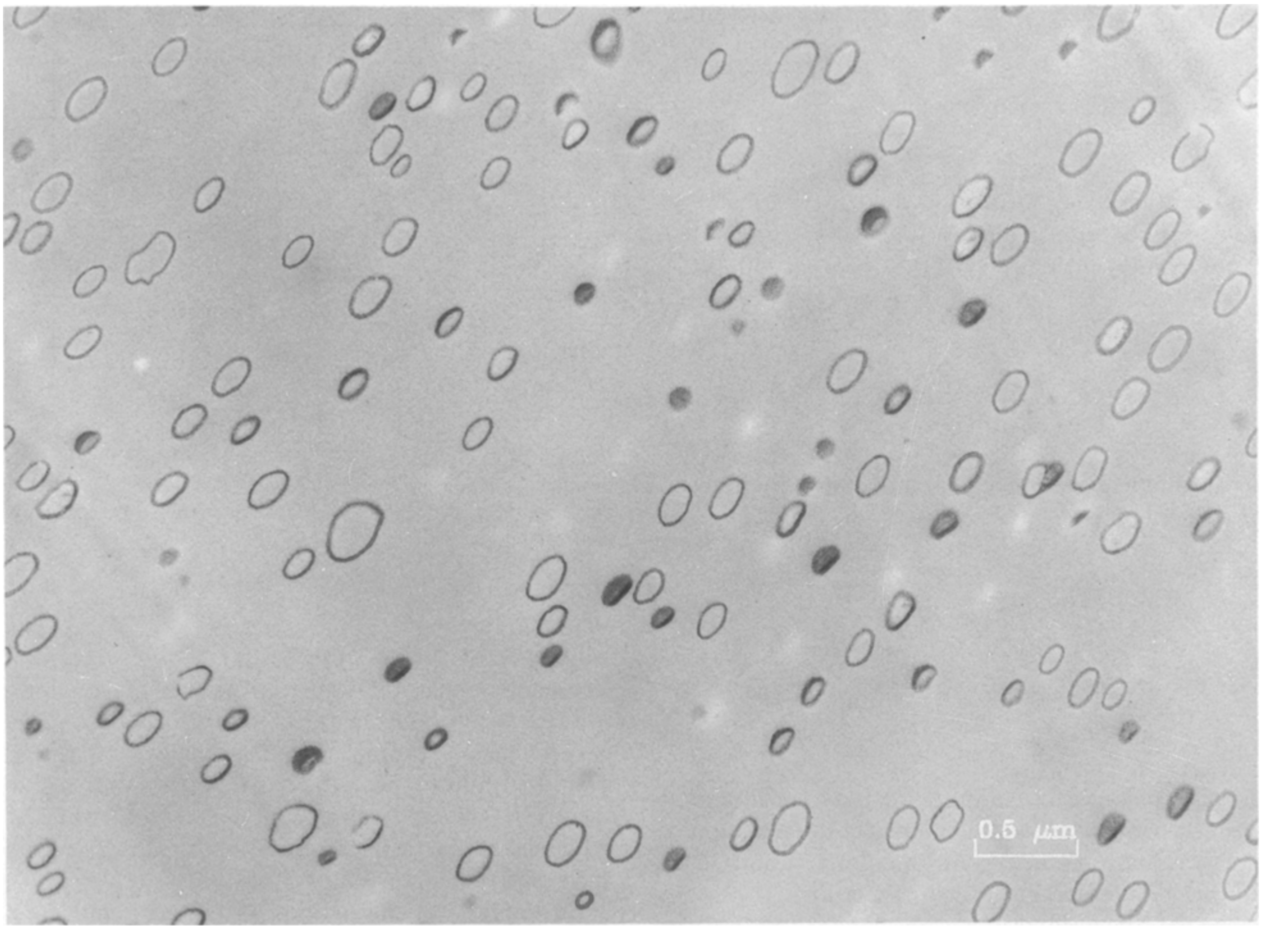

Figure 10 TEM micrograph of HIPS2 from a slice exhibiting a silver interference colour corresponding to a thickness of about 0.075 μm.

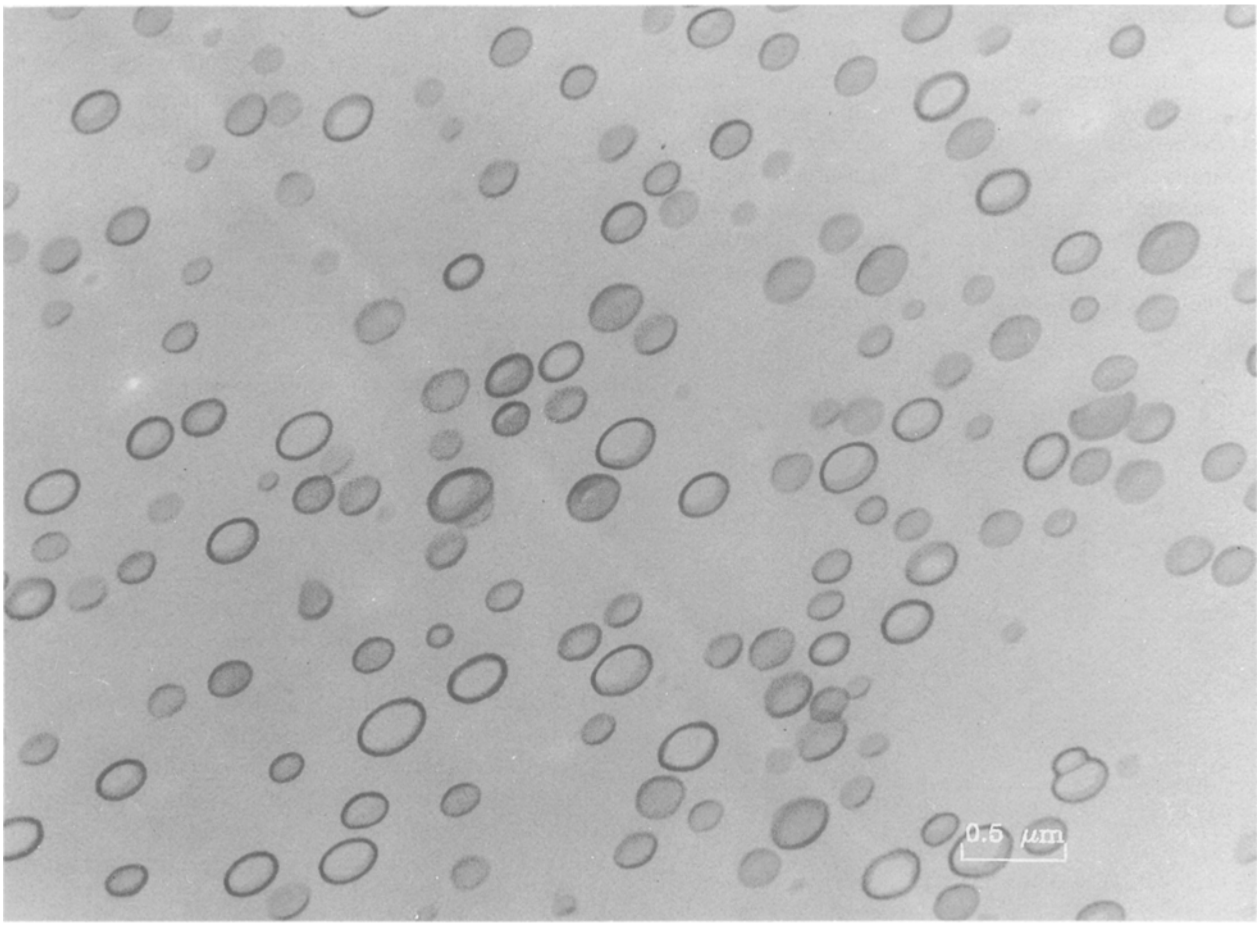

Figure 11 TEM micrograph of HIPS2 from a slice exhibiting a green interference colour corresponding to a thickness of about 0.260 μm.

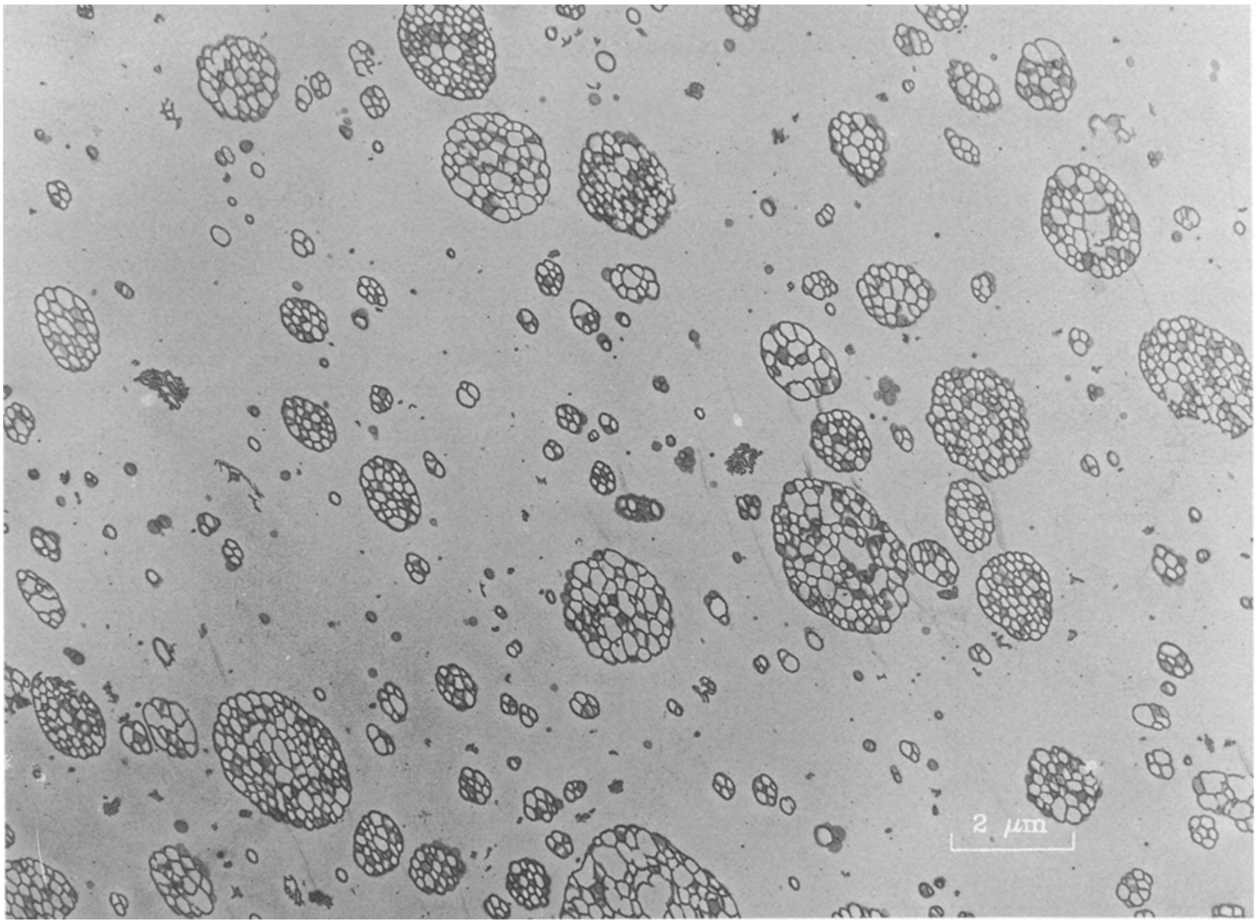

Figure 12 TEM micrograph of HIPS1 from a slice exhibiting a gold interference colour corresponding to a thickness of about 0.120 μm.

two complete series of materials, indicated as HIPS1(1), HIPS1(2), HIPS1(3), HIPS1(4) and HIPS2(1), HIPS2(2), HIPS2(3), HIPS2(4), were obtained by melt mixing in increasing proportions PS homopolymer (having approximately the same molecular characteristics as the matrices in the two original materials) in order to obtain materials with dispersed phases in the proportion of 1, 3/4, 1/2 and 1/4 with respect to the original ones.

TABLE I Slice thickness associated with different interference colour according to Ref. 33

Interference colour	Thickness (μm)
Silver	0.075
Gold	0.120
Purple	0.170
Blue	0.215
Green-yellow	0.260

5.2. Second phase volume fraction and particle size distribution determination by means of image analysis

For each material of the two series, several TEM micrographs from samples having different thickness were taken. The slices were cut using an ultramicrotome and the thickness was determined by floating the cut slice on the water surface, estimating the interference colour (Table I shows the thickness associated with different interference colours) [33]. Slices showing more than one, unambiguous interference colour were not considered. Before the microtoming all the samples were immersed in an aqueous solution of OsO_4 for 2 days; as explained before, the staining procedure facilitates the cutting.

The cut slices were observed and photographed using an 100 kV TEM, taking care not to excessively condense the electron beam. This ensured that no deformation due to heating by electron absorption took place inside the samples. For each material and for each slice thickness the number of pictures taken was sufficient always to examine more than 400 particle sections. The micrographs were then analysed using a computerized Nachet-Vision image analysis system. Using a grey scale the particle sections were first separated from the background constituted by the PS matrix, then, by means of an appropriate use of filling and erosion routines, the particle sections, including their inner sub-inclusions, were delimited and individually considered. This procedure introduced cuts in correspondence to overlapped regions that, however, were always few and reduced in area in all the samples considered (see Appendix 2).

Assuming that all the particles were perfectly circular, which was quite true because the bulk samples had been preventitively thermally treated in order to avoid anisotropy due to molecular orientation, the apparent radius r_i of each particle section was computed as:

$$r_i = \left(\frac{S_i}{\pi}\right)^{1/2} \qquad (73)$$

where S_i was the particle section surface obtained, by means of a straightforward calibration, from its number of pixels. The moments $\langle r^b \rangle$ (b is a positive integer) were computed according to the previously mentioned formulae and the apparent second phase volume fraction simply as the ratio between the number of pixels imaging the particles and the total number of pixels.

In Tables II and III, for each material and for each specimen thickness, the values of the first two section radius distribution moments, of the apparent volume fraction and of the number of observed particles are reported. It is easy to observe that a general trend exists in the data of ϕ_{app} measured on the same material with specimens having different thickness: ϕ_{app} increases and it can also double when the thickness is varied from about 0.07 μm to about 0.25 μm. A less pronounced trend exists also in the distribution moments that tend to increase too, increasing the specimen thickness.

Equations 23, 24 and 25 have now to be applied to this practical case: because there are five different measurements made corresponding to five different thicknesses, we are dealing with an overdetermined system of equations. It is important to stress, at this point, that the determination of the distribution moments $\langle R^a \rangle$ ($a = 1, 2, 3$) does not depend on the second phase volume fraction value, but only on the thickness of the examined section. In fact, if a large enough section is observed and then a sufficient number of particles, the section radius distribution is the same, independently of the volume fraction: in other words, one must obtain the same values of $\langle R^a \rangle$ analysing pictures coming from a sample with different volume fraction values, but with the same thickness. Then the precision in the computation of $\langle R^a \rangle$ can be increased simply by considering, for HIPS1 and HIPS2, an average of the data coming from samples having the same thickness, not considering the second phase volume fraction. Thus can be derived from the data only one system of equations for HIPS1 and one for HIPS2, concerning a very large number of measured particles sections (in Tables II and III the averaged values and the system equations are also displayed). Applying the least squares method, the

TABLE II Image analysis data for HIPS1

Thickness, t (μm)	Material	Observed particles	$\langle r^1 \rangle$ (μm)	$\langle r^2 \rangle$ (μm²)	ϕ_{app}	$\overline{\langle r^1 \rangle}$ (μm)	$\overline{\langle r^2 \rangle}$ (μm²)	ϕ
0.075	HIPS1(1)	368	0.239	0.102	0.0742			0.0677
0.075	HIPS1(2)	587	0.216	0.083	0.1489			0.1358
0.075	HIPS1(3)	535	0.190	0.070	0.2121			0.1935
0.075	HIPS1(4)	782	0.235	0.096	0.2763	0.220	0.087	0.2520
0.120	HIPS1(1)	466	0.229	0.094	0.0750			0.0650
0.120	HIPS1(2)	578	0.226	0.101	0.1494			0.1295
0.120	HIPS1(3)	539	0.228	0.105	0.2369			0.2053
0.120	HIPS1(4)	644	0.227	0.110	0.3010	0.227	0.103	0.2608
0.170	HIPS1(1)	368	0.242	0.110	0.0867			0.0712
0.170	HIPS1(2)	558	0.216	0.091	0.1492			0.1225
0.170	HIPS1(3)	535	0.237	0.105	0.2312			0.1898
0.170	HIPS1(4)	1000	0.209	0.086	0.2905	0.222	0.095	0.2385
0.215	HIPS1(1)	385	0.243	0.122	0.0865			0.0678
0.215	HIPS1(2)	503	0.231	0.112	0.1809			0.1417
0.215	HIPS1(3)	518	0.242	0.102	0.2309			0.1810
0.215	HIPS1(4)	913	0.237	0.108	0.3163	0.238	0.110	0.2479
0.260	HIPS1(1)	407	0.205	0.088	0.1005			0.0753
0.260	HIPS1(2)	512	0.247	0.115	0.1797			0.1347
0.260	HIPS1(3)	590	0.235	0.111	0.2616			0.1961
0.260	HIPS1(4)	902	0.227	0.098	0.3297	0.230	0.103	0.2472

Equations 23, 24 and 25 give rise to the following ten equations

$$-0.730\langle R^1 \rangle + 3.141\langle R^2 \rangle = 0.330$$
$$-0.526\langle R^1 \rangle + 0.225\langle R^2 \rangle + 4\langle R^3 \rangle = 0.020$$
$$-0.670\langle R^1 \rangle + 3.141\langle R^2 \rangle = 0.055$$
$$-0.617\langle R^1 \rangle + 0.360\langle R^2 \rangle + 4\langle R^3 \rangle = 0.037$$
$$-0.547\langle R^1 \rangle + 3.141\langle R^2 \rangle = 0.075$$
$$-0.569\langle R^1 \rangle + 0.510\langle R^2 \rangle + 4\langle R^3 \rangle = 0.048$$
$$-0.521\langle R^1 \rangle + 3.141\langle R^2 \rangle = 0.102$$
$$-0.658\langle R^1 \rangle + 0.645\langle R^2 \rangle + 4\langle R^3 \rangle = 0.071$$
$$-0.397\langle R^1 \rangle + 3.141\langle R^2 \rangle = 0.119$$
$$-0.618\langle R^1 \rangle + 0.780\langle R^2 \rangle + 4\langle R^3 \rangle = 0.080$$

from which, applying the least squares method described in the text, it is possible to obtain

$\langle R^1 \rangle = 0.240$ μm, $\langle R^2 \rangle = 0.069$ μm², $\langle R^3 \rangle = 0.040$ μm³, and $\beta^2 = 0.184$ $\gamma = 16.628$. Using these values, together with data of ϕ_{app}, one can easily compute from Equation 25 the values of ϕ displayed in the table.

TABLE III Image analysis data for HIPS2

Thickness, t (μm)	Material	Observed particles	$\langle r^1 \rangle$ (μm)	$\langle r^2 \rangle$ (μm^2)	ϕ_{app}	$\overline{\langle r^1 \rangle}$ (μm)	$\overline{\langle r^2 \rangle}$ (μm^2)	ϕ
0.075	HIPS2(1)	433	0.0782	0.0068	0.0518			0.0340
0.075	HIPS2(2)	471	0.0795	0.0069	0.0849			0.0556
0.075	HIPS2(3)	670	0.0867	0.0083	0.1463			0.0959
0.075	HIPS2(4)	722	0.0845	0.0078	0.2020	0.0829	0.0076	0.1324
0.120	HIPS2(1)	339	0.0843	0.0078	0.0562			0.0305
0.120	HIPS2(2)	421	0.0927	0.0093	0.1028			0.0558
0.120	HIPS2(3)	603	0.0896	0.0089	0.1462			0.0794
0.120	HIPS2(4)	681	0.0823	0.0075	0.1796	0.0869	0.0083	0.0975
0.170	HIPS2(1)	363	0.0904	0.0090	0.0700			0.0319
0.170	HIPS2(2)	405	0.0990	0.0106	0.1140			0.0520
0.170	HIPS2(3)	550	0.0947	0.0100	0.1502			0.0685
0.170	HIPS2(4)	653	0.0907	0.0091	0.2141	0.0935	0.0096	0.0977
0.215	HIPS2(1)	342	0.0971	0.0103	0.0769			0.0307
0.215	HIPS2(2)	487	0.0964	0.0101	0.1316			0.0525
0.215	HIPS2(3)	627	0.0983	0.0106	0.1819			0.0726
0.215	HIPS2(4)	658	0.0943	0.0098	0.2384	0.0964	0.0102	0.0951
0.260	HIPS2(1)	336	0.0973	0.0102	0.0749			0.0265
0.260	HIPS2(2)	490	0.1020	0.0112	0.1466			0.0519
0.260	HIPS2(3)	1186	0.1030	0.0117	0.2261			0.0801
0.260	HIPS2(4)	584	0.1030	0.0119	0.2550	0.1021	0.0115	0.0903

Equations 23, 24 and 25 give rise to the following ten equations

$$
\begin{aligned}
&-0.1816\langle R^1\rangle + 3.141\langle R^2\rangle = 0.0124\\
&-0.0454\langle R^1\rangle + 0.225\langle R^2\rangle + 4\langle R^3\rangle = 0.0017\\
&-0.1076\langle R^1\rangle + 3.141\langle R^2\rangle = 0.0209\\
&-0.0500\langle R^1\rangle + 0.360\langle R^2\rangle + 4\langle R^3\rangle = 0.0030\\
&-0.0338\langle R^1\rangle + 3.141\langle R^2\rangle = 0.0318\\
&-0.0578\langle R^1\rangle + 0.510\langle R^2\rangle + 4\langle R^3\rangle = 0.0049\\
&-0.0442\langle R^1\rangle + 3.141\langle R^2\rangle = 0.0415\\
&-0.0614\langle R^1\rangle + 0.645\langle R^2\rangle + 4\langle R^3\rangle = 0.0066\\
&-0.1115\langle R^1\rangle + 3.141\langle R^2\rangle = 0.0531\\
&-0.0687\langle R^1\rangle + 0.780\langle R^2\rangle + 4\langle R^3\rangle = 0.0089
\end{aligned}
$$

from which, applying the least squares method described in the text, it is possible to obtain

$\langle R^1\rangle = 0.1372$ μm, $\langle R^2\rangle = 0.0117$ μm^2, $\langle R^3\rangle = 0.0017$ μm^3, and $\beta^2 = -0.380$. Assuming that $\langle R^2\rangle = \langle R^1\rangle^2$ and $\langle R^3\rangle = \langle R^1\rangle^3$ (monomodal distribution) each one of the ten equations reported above can be solved. Averaging all the solutions one obtains a mean value and a standard deviation: $\langle R^1\rangle = 0.1070$, $\sigma(\langle R^1\rangle) = 0.0060$. Using these values, together with the data of ϕ_{app}, one can easily compute from Equation 25 the values of ϕ displayed in the table.

values of $\langle R^a\rangle$ for HIPS1 and HIPS2 are easily obtainable and they are also displayed in Tables II, and III.

HIPS1 shows a broad, positively skewed particle size distribution. The solution values $\langle R^a\rangle$ for HIPS2 are, on the other hand, not satisfactory: the value of β^2 is negative which is without any geometrical meaning. The mathematical reason for this drawback lies in the fact that the least squares method does not exclude solutions: in principle, for example, it could choose a solution in which one of the moments is negative. As we mentioned, using the simplex algorithm, one can introduce further conditions in the system resolution, like, for example, that the moments $\langle R^a\rangle$ and β^2 should all be positive. Our purpose, however, is to keep the solution of the system as simple as is acceptable: more simply, then, one can imagine that the best-fitting non-contradictory HIPS2 distribution should be extremely narrow and attempt to solve the system assuming the particle size distribution monomodal. So, taking Equation 5 into account, for each of the ten equations concerning HIPS2 it is possible to obtain a value of R and then to mediate between them. In Tables II and III the mean value of the solution is always displayed, together with its standard deviation which is of about 5% and more than satisfactory for this kind of measurement, confirming that the assumption of monomodal distribution is reasonable.

Now that the values of $\langle R^a\rangle$ for the two materials have been obtained, the value of ϕ for each specimen thickness can be computed. These values are displayed in Tables II and III. It is easy to observe that, for each material of the two series, the application of the mathematical treatment to the values of ϕ_{app} obtained from differently thick samples gives rise to values of ϕ which contain little or no scattering, confirming the validity of the approach.

5.3. Second phase volume fraction determination by means of a selective solvents separation method

For each material of the two series the measurements of the second phase volume fraction have been made following the method previously described in Reference 3.

5.4. Second phase volume fraction determination by means of an indirect method

For each material of the two series, measurements of the Young's modulus E in three-point bending and dual cantilever geometries and of the shear modulus G in torsion have been performed. The measurements were made using, respectively, a Rheometrics RSA II and a Rheometrics RMS 800 on specimens obtained from compression-moulded plates. The moduli were measured in a dynamic regime with sinusoidal strain pulses of about 0.05% at a frequency of about 6.3 rad s^{-1}. The data are displayed in Table IV.

5.5. Discussion

Table IV summarizes the results obtained for each material in the two series by applying the three different methods for the determination or estimation of ϕ.

First, data from the proposed image analysis method and from the separation procedure are compared. Fig. 13 shows a plot of the second phase volume fraction values obtained from the image analysis, indicated as ϕ_{IA}, and those from the separation procedure, indicated as ϕ_s. From the figure it is easy to conclude that $\phi_{IA} > \phi_s$ for HIPS1 and $\phi_{IA} < \phi_s$ for HIPS 2. A possible explanation of this fact, not completely unexpected, can be traced in some of the features of the separation process that, as we anticipated, have been in the past somewhat neglected or overlooked. In the separation process, for instance, it can happen that not all the second phase is separated properly and that the material inside the sub-inclusions is extracted. Also, the PS part of the interfacial matter is computed in the gel measurements, while it is not in the image analysis method. So, we believe these facts to be the most reasonable cause of the data discrepancy showed in Fig. 13.

One can imagine that in HIPS2 the PS interfacial matter could be relatively higher than in HIPS1, giving rise to higher values of the second phase volume fraction computed using the separation procedure, while it is possible that not all the HIPS1 particles would have been well centrifuged or that a non-negligible amount of material would have been extracted from the sub-inclusions. A more accurate investigation of the causes of these discrepancies is definitely needed, however it is not essential to this paper.

It is interesting at this point to check if the previously reported experimental evidence of the dependency of the elastic modulus only on the second phase volume fraction is also confirmed by our data. Cigna [3] drew his results plotting the values of G modulus versus the second phase volume fraction obtained by his separation method: he considered materials having big particles with salami structures formed during the polymerization process or bulk rubber particles obtained by simple melt mixing and found quite a good correlation showing that ϕ_s is the only parameter affecting G. Doing the same, plotting our values of G versus the values of ϕ_s, we find that the two materials data split in two different sets (see Fig. 14, which also contains the data from Ref. 3): to have HIPS1 and HIPS2 with the same shear modulus one needs to consider the HIPS2 with greater ϕ_s (the situation is essentially the same if one considers the Young's modulus E). This fact, however, is not sufficient to affirm that G does not depend only on the rubbery phase volume fraction: ϕ_s, as mentioned above, probably measures different characteristics in structurally different materials and, while it would have been a convenient estimation of the rubbery phase volume fraction for Cigna's homogeneous set of materials and for HIPS1, it is not for HIPS2.

The values of ϕ_{IA} seem plausibly more appropriate to be plotted versus G. Nevertheless the splitting of data still occurs, the situation being completely reversed with respect to the previous case: HIPS1 has a greater ϕ_{IA} than HIPS2 when the modulus is constant (see Fig. 15). The fact that some mathematical simplifications are involved in the computation of ϕ_{IA}, for example the assumption that the particles considered should be perfectly spherical, and that these simplifications can introduce some systematic errors, is not sufficient, in our opinion, to account for the data splitting concerning HIPS1 and HIPS2 shown in Fig. 15 that must be imputed to differences existing in the two sets of materials.

So, despite the existence of a general trend relating G and ϕ, however this parameter has been measured, the last results induce one to believe that a strict relationship cannot be found when the materials under investigation contain rubbery phases having

TABLE IV Second phase volume fraction from different experimental procedures and elastic moduli data

Material	Volume fraction ϕ_{IA}, by image analysis	Volume fraction ϕ_s by separation	Young's modulus, E, by 3-point bending (MPa)	Young's modulus, E, by dual cantilever (MPa)	Shear modulus, G (MPa)
HIPS1(1)	0.0694	0.044	2849	2795	1163
HIPS1(2)	0.1328	0.092	2500	2436	1022
HIPS1(3)	0.1931	0.144	2177	2143	857
HIPS1(4)	0.2493	0.192	1886	1933	736
HIPS2(1)	0.0307	0.047	2945	2907	1256
HIPS2(2)	0.0536	0.097	2763	2654	1127
HIPS2(3)	0.0793	0.145	2555	2452	1049
HIPS2(4)	0.1026	0.196	2376	2341	934

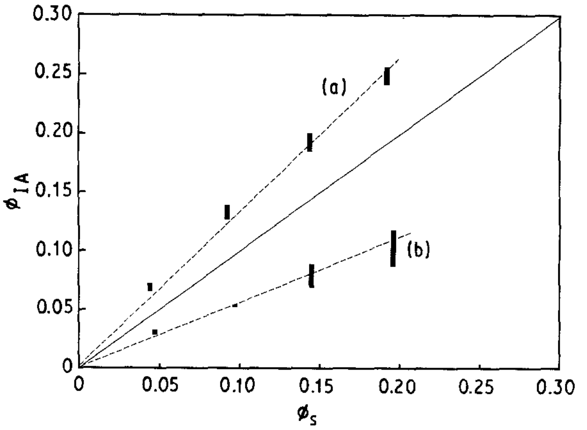

Figure 13 Plot of the second phase volume fraction data obtained from image analysis versus those obtained by the Cigna separation procedure for (a) HIPS1 and (b) HIPS2. The continuous line represents $\phi_{IA} = \phi_s$, the dashed lines are guides for the eye.

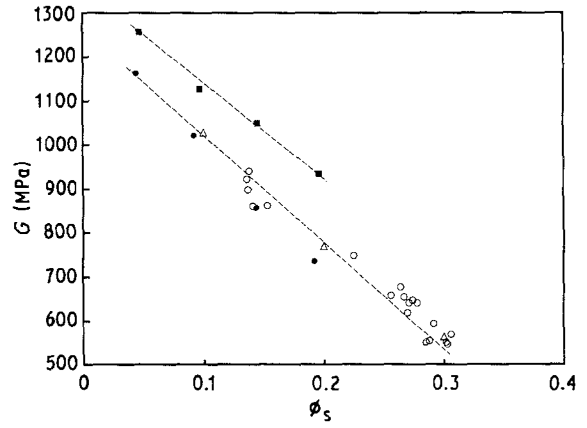

Figure 14 Plot of the shear modulus G versus the values of second phase volume fraction obtained from the Cigna separation procedure. (●) HIPS1; (■) HIPS2; (○) HIPS containing particles with salami structures (data from Reference 3); (△) HIPS containing bulk rubber particles obtained from melt-mixing (data from Reference 3). The dashed lines are guides for the eye.

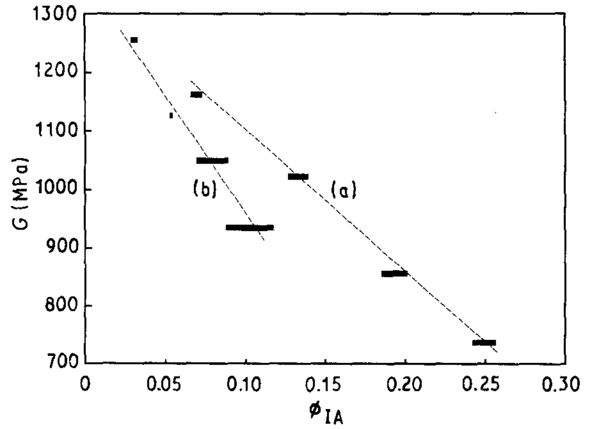

Figure 15 Plot of the shear modulus G versus the values of second phase volume fraction obtained from image analysis of (a) HIPS1 and (b) HIPS2. The dashed lines are guides for the eye.

extremely different morphological and structural characteristics, as in the case of HIPS1 and HIPS2. The mechanical elastic behaviour of the two materials appears to be influenced by variables which are not well accounted for either in ϕ_s or in ϕ_{IA}, the size, structure and morphology of the particles playing most likely a very fundamental role. Bucknall [30] already showed data of HIPS having the same rubbery volume fraction and different moduli, accounting for this fact with the different structure and morphology of the rubber particles which could be responsible for quite a large variation of the moduli of the particles themselves. Regardless of the fact that his second phase volume fraction measurements are dubious, we can share here his assessment: assuming that the materials behave as if they contain entirely soft inclusions (having a volume fraction equal to ϕ_{IA} or ϕ_s), not taking into account the large differences in the particle structure, seems to yield a broad approximation.

6. Conclusions

The determination of the second phase volume fraction and of the particle size distribution is extremely important and necessary in many rubber-toughened polymers containing the toughening agents in the form of small, soft particles randomly dispersed in the matrix.

HIPS is a good model system for such materials: generally the rubber phase forms during the polymerization process and its features have to be determined *a posteriori*.

The determination procedures of the rubbery phase features in HIPS have been briefly reviewed, with particular attention to the separation procedures, to microscopic methods involving some image analysis methodology and to indirect estimations concerning mechanical measurements, showing how some factors have always been neglected or overlooked.

A simple method to be used in the image analysis of micrographs, based on an elementary stereological assumption has been proposed: attention has been focused on the ratio between the mean particle radius and the thickness of the observed specimen. The method can give useful results when samples with different thickness are examined.

The method has been successfully tested using a computer simulation routine which gave results well in agreement with the theoretical relationships.

The proposed method, together with a standard separation procedure and indirect mechanical measurements, has been tested experimentally on two series of HIPS having particles with different size and structures.

One of the results of this experimental investigation suggests that approximated views relating elastic properties of HIPS (and more generally of rubber-toughened polymers) only to the rubber particle volume fraction, however it has been measured, are possibly questionable.

Acknowledgements

The authors are grateful to G. Cigna, P. Lomellini, L. Castellani and G. P. Ravanetti for valuable discussions and for assistance in performing the mechanical measurements (P. L. and L. C.), to F. Gandini and

M. Lucchini for the drawings, and to K. Pisoni and P. Sarto for their kind and continuous collaboration.

Appendix 1. Derivation of Equations 23, 24 and 25

Let us start by considering M particles, the ith of them having radius R_i and the radii being distributed following a given $F(R)$. Using the same argument expressed in the text, one can recognize that the sections on a large enough slice of thickness t are distributed as the sections cut by planes on the composite figure composed by M parts, each formed by two half-spheres having radius R_i and by a central cylinder having the same radius and height equal to t.

Consider now the ith of these figures cut by N_i parallel planes equally spaced with a distance ε

$$N_i\varepsilon = 2R_i + t \tag{A1}$$

The fact that the number of figures considered is now M implies that Equations 12 and 13 have to be generalized in the following form:

$$\begin{aligned}
A_{\text{tot}} &= \sum_{i=1}^{M} A_i = \sum_{i=1}^{M} (\pi R_i^2 + 2tR_i) \\
&= M(\pi\langle R^2\rangle + 2t\langle R^1\rangle) \sim \sum_{i=1}^{M}\sum_{j=1}^{N_i} 2\varepsilon r_{(i)j} \\
&= \sum_{i=1}^{M} 2\varepsilon N_i \left(\frac{\sum_{i=1}^{M}\sum_{j=1}^{N_i} r_{(i)j}}{\sum_{i=1}^{M} N_i}\right) \\
&= \left(\sum_{i=1}^{M} 2\varepsilon N_i\right)\langle r^1\rangle
\end{aligned} \tag{A2}$$

$$\begin{aligned}
V_{\text{tot}} &= \sum_{i=1}^{M} V_i = \sum_{i=1}^{M}\left(\frac{4\pi R_i^3}{3} + \pi t R_i^2\right) \\
&= M\left(\frac{4\pi\langle R^3\rangle}{3} + \pi t\langle R^2\rangle\right) \\
&\sim \sum_{i=1}^{M}\sum_{j=1}^{N_i} \varepsilon(\pi r_{(i)j}^2) = \sum_{i=1}^{M} \varepsilon N_i \pi \left(\frac{\sum_{i=1}^{M}\sum_{j=1}^{N_i} r_{(i)j}^2}{\sum_{i=1}^{M} N_i}\right) \\
&= \left(\sum_{i=1}^{M} \varepsilon N_i \pi\right)\langle r^2\rangle
\end{aligned} \tag{A3}$$

where A_{tot} is the total (vertical) surface area, V_{tot} the total volume of the composite figure, $r_{(i)j}$ represents the jth section radius of the ith particle and the definitions of the moments have been modified as follows

$$\langle R^a\rangle = \frac{\sum_{i=1}^{M} R_i^a}{M} \tag{A4}$$

$$\langle r^b\rangle = \frac{\sum_{i=1}^{M}\sum_{j=1}^{N_i} r_{(i)j}}{\sum_{i=1}^{M} N_i} \tag{A5}$$

Using Equations A1, A4 and A5, Equations A2 and A3 can be easily transformed into Equations 23 and 24.

Equation 25 can be derived following exactly the same procedure adopted in the text, taking into account that the value of $\langle r^2\rangle$ is now expressed by Equation A3 and that the proper definition of ϕ in the generic case is

$$\phi \sim \frac{4\pi M\langle R^3\rangle}{3L^3} \tag{A6}$$

The outlines of the derivation of Equations A2 and A3 admit a generalization that allows the calculation of the generic $\langle r^b\rangle$ with $b > 2$ and then to obtain further information about the geometrical features of the distribution, such as its kurtosis. In fact it is true that

$$\begin{aligned}
&\Theta_n(\langle R^n\rangle) + t\Theta_{n-1}(\langle R^{n-1}\rangle) \\
&\quad = (2\langle R^1\rangle + t)\Theta_{n-1}(\langle r^{n-1}\rangle)
\end{aligned} \tag{A7}$$

where $\Theta_k(\langle R^k\rangle)$ is given by

$$\Theta_k(\langle R^k\rangle) = \frac{2^k\pi^{\text{int}(k/2)}}{\prod_{i=\text{even/odd}}^{k} i}\langle R^k\rangle \tag{A8}$$

where $\text{int}(k/2)$ means the integer part of $k/2$ and the product sign Π is intended only on the even i when k is even and on the odd i when k is odd (from a geometric point of view $\Theta_k(\langle R^k\rangle)$ is the volume of the k-dimensional sphere having radius $(\langle R^k\rangle)^{1/k}$).

Appendix 2. Overlapping particle sections

Equations 23, 24 and 25 have been derived supposing phantom particles, i.e. particles which can be interpenetrated. Clearly, this is not a realistic condition, however Equations 23 and 24 do not change their appearance if one introduces the non-overlapping requirement

$$\forall i, \forall j = 1, 2, 3, \ldots M$$

$$\left(\sum_{k=1}^{3}(x_k(i) - x_k(j))^2\right)^{1/2} > R_i + R_j \tag{A9}$$

where i and j are indices labelling the particles, $(x_1(i), x_2(i), x_3(i))$ and $(x_1(j), x_2(j), x_3(j))$ are the Cartesian coordinates in a given frame of the ith and jth particle centres and R_i and R_j their radii (Equation A9 is equivalent to Equation 62 introduced as a condition in the simulation program).

The situation concerning ϕ_{app} and ϕ is more complex: also if Equation A9 is verified, the particle sections in a micrograph from a thick sample can be overlapped and the definition of the apparent volume fraction must take into account this overlapping. It is now understandable that the mathematical model developed computes the parameter ϕ_{app} as

$$\phi_{\text{app}} = \frac{\sum_{j=1}^{N}\mu(A_j)}{L^2} = \frac{\sum_{j=1}^{N}\pi r_j^2}{L^2} \sim \frac{\pi N\langle r^2\rangle}{L^2}. \tag{A10}$$

where A_j represents the single jth particle projection on the considered section and r_j and $\mu(A_j)$ its radius and its Cartesian measure, respectively. (N is the particles number in the section and L^2 the total section area.) However, from an experimental point of view, it is extremely difficult to resolve the contribution of a single particle in a cluster of two or more overlapped particles*, then the parameter generally measured using the standard image analysis methods is $\phi^{(e)}_{\mathrm{app}}$, definable as

$$\phi^{(e)}_{\mathrm{app}} = \frac{\mu\left(\bigcup_{j=1}^{N} A_j\right)}{L^2} \qquad \text{(A11)}$$

where $\bigcup_{j=1}^{N} A_j$ represents the union of all the A_j.
It is possible to demonstrate that

$$\phi^{(e)}_{\mathrm{app}} = \phi_{\mathrm{app}} - \frac{\mu\left(A_i \bigcap_{i>j}^{N} A_j\right) - \mu\left(A_i \bigcap_{i>j}^{N} A_j \bigcap_{j>k}^{N} A_k\right) + \mu\left(A_i \bigcap_{i>j}^{N} A_j \bigcap_{j>k}^{N} A_k \bigcap_{k>h}^{N} A_h\right) - \ldots}{L^2} \qquad \text{(A12)}$$

The two parameters ϕ_{app} and $\phi^{(e)}_{\mathrm{app}}$ are then similar only when a small number of intersected (overlapped) particles is contained in the examined pictures, i.e. when thin sections and/or materials having very low second phase volume fraction values are under investigation.

Despite the laborious nature of the analytical computation of A12, it is important, at this point, to assess quantitatively how the overlapping depends on the variables introduced. Clearly when the examined section thickness is well below the average particle radius no overlapping is possible and then $\phi^{(e)}_{\mathrm{app}}$ and ϕ_{app} tend to coincide, while, when the section thickness is much larger than the particle radius, one can imagine that, at least for monomodal distributions, the ratio $\phi_{\mathrm{app}}/\phi^{(e)}_{\mathrm{app}}$ scales as ϕ/τ. No easy guess, however, is possible in the intermediate region, which is the one of greater experimental interest.

A possible way to avoid these obstacles is the numerical modelling of the problem. Equation 72 used for the computation of ϕ_{app} in the numerical simulation does not take into account the possible overlapping between particle sections, in perfect analogy with the theoretical Equation 25, nonetheless the numerical simulation represents the simplest way available to estimate quantitatively the effect of overlapping. To do that we introduced in the previously described program a simple routine. The generic section was considered to be a square having linear dimension equal L, inside which can be constructed a grid having $N_c \times N_c$ squared cells and, for each generic kth cell, we can consider the two-dimensional coordinates of its centre $(x^c_1(k), x^c_2(k))$. We assume that, if this centre point of the cell is contained at least in one particle section, the entire cell has to be considered occupied by the second phase. Mathematically the kth cell has to be accounted if

$$\exists j \qquad \left(\sum_{i=1}^{2} (x_i(j) - x^c_i(k))^2\right)^{1/2} \leq r_j \qquad \text{(A13)}$$

The computation of the apparent volume fraction $\phi^{(e)}_{\mathrm{app}}$ defined as in Equation A11 is simply given by the ratio between the number N_0 of the occupied cells and the total number of cells $N_c \times N_c$. Of course the accuracy of this computation increases as the linear dimension of the squared cells decreases or, which is equivalent, N_c increases.

Fig. A1 shows a plot of $\phi^{(e)}_{\mathrm{app}}/\phi_{\mathrm{app}}$ computed from the above described routine versus ϕ/τ for simulated materials having particles with monomodal distribution in size. As expected, $\phi^{(e)}_{\mathrm{app}}/\phi_{\mathrm{app}}$ is very close to unity when ϕ/τ is low, while it scales as ϕ/τ for high values of ϕ/τ.

From an experimental point of view, on the other hand, one can obtain merely $\phi^{(e)}_{\mathrm{app}}$ and τ and not the value of ϕ until the computation of ϕ_{app}. So, it is interesting to plot the ratio $\phi^{(e)}_{\mathrm{app}}/\phi_{\mathrm{app}}$ versus $\phi^{(e)}_{\mathrm{app}}/\tau$ in order to estimate ϕ_{app} from known quantities. Fig. A2 shows such a plot for the same data displayed in Fig. A1. The arrow indicates the maximum experimental ascissa obtained from our experimental samples, confirming that the data we collected were distinguished by no or very low overlapping.

Fig. A2 demonstrates that the overlapping is not important until the parameter $\phi^{(e)}_{\mathrm{app}}/\tau$ is greater than unity. Subsequently, increasing $\phi^{(e)}_{\mathrm{app}}/\tau$, the overlapping quickly becomes critical, making the estimation of ϕ_{app} and then of ϕ practically unattainable. A consequence of this result is that the quantitative

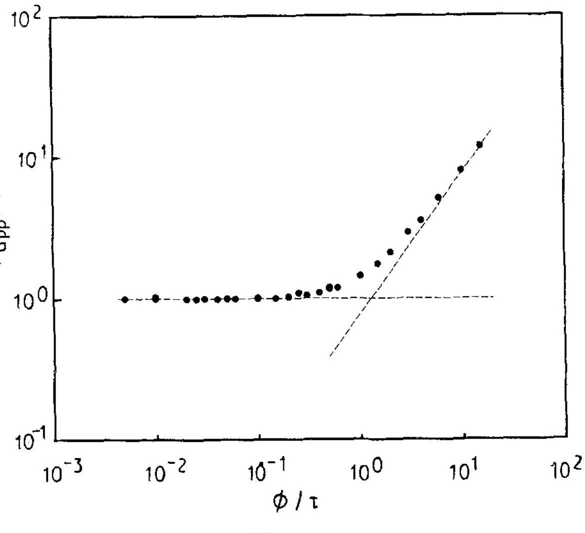

Figure A1 Log–log plot of $\phi^{(e)}_{\mathrm{app}}/\phi_{\mathrm{app}}$ versus ϕ/τ. The symbols are data from the numerical simulation. For large values of ϕ/τ the plot exhibits a slope of approximately unity, demonstrating that $\phi^{(e)}_{\mathrm{app}}/\phi_{\mathrm{app}}$ scales as ϕ/τ.

---

* Some sophisticated image analysis systems can obtain estimations of ϕ_{app} because they are able to create an hierarchy in the contrasts of the examined image. However, this estimation becomes more approximate when the number of overlapped particles and/or the thickness of the examined section are very large.

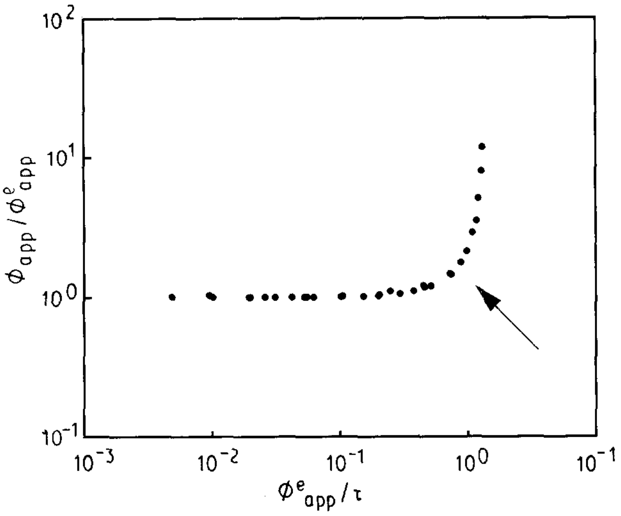

Figure A2 Log–log plot of $\phi^{(e)}_{app}/\phi_{app}$ versus $\phi^{(e)}_{app}/\tau$. The symbols are data from the numerical simulation. The arrow indicates the region of $\phi^{(e)}_{app}/\tau$ in which the larger experimental values that we obtained are contained.

analysis of optical micrographs for which $\phi^{(e)}_{app}/\tau$ assumes values significantly greater than unity is highly questionable.

References

1. C. B. BUCKNALL, "Toughened Plastics" (Applied Science, London, 1977).
2. A. ECHTE, in "Rubber Toughened Plastics", edited by C. K. Riew (American Chemical Society, Washington, 1989).
3. G. CIGNA, *J. Appl. Polym. Sci.* **14** (1970) 1781.
4. G. CIGNA, P. LOMELLINI and M. MERLOTTI, *ibid.* **37** (1989) 1527.
5. C. B. BUCKNALL, D. CLAYTON and W. E. KEAST, *J. Mater. Sci.* **7** (1972) 1443.
6. A. M. DONALD and E. J. KRAMER, *J. Polym. Sci.* **27** (1982) 3729.
7. R. E. LAVENGOOD, US Patent 4214056 (1980).
8. S. Y. HOBBS, *Polym. Eng. Sci.* **26** (1986) 74.
9. H. KESSKULA, in "Rubber Toughened Plastics", edited by C. K. Riew (American Chemical Society, Washington, 1989).
10. N. R. RUFFING, US Patent 3243481 (1966).
11. R. A. HALL, R. D. HITES and P. PLANTZ, *J. Appl. Polym. Sci.* **27** (1982) 2885.
12. D. E. JAMES, *Polym. Eng. Sci.* **8** (1968) 241.
13. T. O. CRAIG, R. M. QUICK and T. E. JENKINS, *J. Polym. Sci. Chem. Edn* **15** (1977) 433.
14. *Idem, ibid.* **15** (1977) 441.
15. G. CIGNA, Private communication.
16. R. A. HALL, *J. Mater. Sci.* **25** (1990) 183.
17. K. KATO, *Polym. Eng. Sci.* **7** (1967) 38.
18. C. V. BERNEY, R. E. COHEN and F. S. BATES, *Polymer* **23** (1982) 1222.
19. E. R. WEIBEL, "Stereological Methods" (Academic Press, New York, 1979).
20. C. B. BUCKNALL, F. F. P. COTE and I. K. PARTRIDGE, *J. Mater. Sci.* **21** (1986) 301.
21. E. E. UNDERWOOD, "Quantitative Stereology" (Addison-Wesley, Reading, Massachusetts, 1970).
22. P. L. GOLDSMITH, *Brit. J. Appl. Phys.* **18** (1967) 813.
23. D. D. WICKSELL, *Biometrica* **17** (1925) 83.
24. *Idem. ibid.* **18** (1926) 152.
25. J. A. SAUER, J. TRENT and C. C. CHEN, *Polym. Eng. Sci.* **29** (1989) 69.
26. R. BUCHDAHL and L. E. NIELSEN, *J. Polym. Sci.* **15** (1955) 1.
27. S. G. TURLEY, *ibid.* **C1** (1963) 101.
28. H. KESKKULA, S. G. TURLEY and R. F. BOYER, *J. Appl. Polym. Sci.* **15** (1971) 351.
29. C. B. BUCKNALL, P. DAVIES and I. K. PARTRIDGE, *J. Mater. Sci.* **21** (1986) 306.
30. *Idem, ibid.* **22** (1987) 1341.
31. T. RICCO', A. PAVAN and F. DANUSSO, *Polym. Eng. Sci.* **18** (1978) 744.
32. L. E. NIELSEN, "Predicting the Properties of the Mixtures" (Marcel Dekker, New York and Basel, 1978).
33. G. DASSU, M. BASSI and G. ALESSANDRINI, "Manuale di Microscopia Elettronica" (Tamburini, Milano, 1967) p. 318.

Received 20 May 1991
and accepted 23 January 1992